AGU PUBLICATIONS

Geochemistry, Geophysics, Geosystems

RESEARCH ARTICLE
10.1002/2015GC005832

Nonlinear attenuation from the interaction between different types of seismic waves and interaction of seismic waves with shallow ambient tectonic stress

Norman H. Sleep[1] and Nori Nakata[1]

[1]Department of Geophysics, Stanford University, Stanford, California, USA

Key Points:
- Strong low-frequency surface waves should suppress high-frequency *S* waves
- Strong *P* waves should suppress reverberating *S* waves
- Stress changes from near-field velocity pulse affect high-frequency *S* waves

Correspondence to:
N. H. Sleep,
norm@stanford.edu

Citation:
Sleep, N. H., and N. Nakata (2015), Nonlinear attenuation from the interaction between different types of seismic waves and interaction of seismic waves with shallow ambient tectonic stress, *Geochem. Geophys. Geosyst.*, *16*, 2336–2363, doi:10.1002/2015GC005832.

Received 30 MAR 2015
Accepted 16 JUN 2015
Accepted article online 19 JUN 2015
Published online 22 JUL 2015

Abstract Strong seismic waves bring rock into frictional failure at the uppermost few hundred meters. Numerous small fractures slip with the cumulative effect of anelastic strain and nonlinear attenuation; these fractures should not distinguish between remote sources of stress. Still, frictional failure criteria are not evident especially when seismic waves change the normal traction on fractures. We identify three earthquakes as examples where consideration of interaction among dynamic stresses from different wave types and ambient tectonic stress provides theoretical predictions of nonlinear attenuation that are potentially testable with single station seismograms. For example, because Rayleigh waves produce shallow horizontal dynamic tension and compression, frictional failure should preferentially occur on the tensile half-cycle if no shallow tectonic stress is present and on the compressional half-cycle if the tectonic stress is already near thrust-faulting failure. We observed neither effect on records from the 2011 M_w 9.0 Great Tohoku earthquake. However, Rayleigh waves from this event appear to have brought rock beneath MYGH05 station into frictional failure at ~10 m depth and thus suppressed high-frequency *S* waves. The tensile half-cycle of high-frequency *P* waves reduced normal traction on horizontal planes beneath station IWTH25 during the 2008 M_w 6.9 Iwate-Miyagi earthquake, weakening the rock in shear and suppressing high-frequency *S* waves. The near-field velocity pulse from the 1992 M_w 7.3 Landers earthquake brought the uppermost few hundred meters of granite beneath Lucerne station into frictional failure, suppressing high-frequency *S* waves. These moderately positive examples support the reality of nonlinear wave interaction, warranting study future strong ground motions.

1. Introduction

Sufficiently strong seismic waves experience nonlinear attenuation as they pass through rocks within the shallow subsurface. One would like to recognize the effects of this process with data, especially single-station seismograms. One would also like to include nonlinear attenuation within mechanical theory that facilitates numerical calculations of the amplitudes of strong seismic waves. In this paper, we present theoretical models for nonlinear attenuation within rock masses with the intent of constraining mechanical behavior.

For introduction, we briefly describe nonlinear attenuation within rocks and relate it to anelastic strain by using scalars. We start with a representation of energy in a seismic wave and attenuation in a linear system. The local elastic strain energy per volume within a seismic wave is $W=\tau\varepsilon/2$, where $\tau=G\varepsilon$ is the dynamic stress, ε is the dynamic elastic strain, and G is the shear modulus. For a propagating wave within a whole space, this energy equals the local kinetic energy per volume $W=\rho V_p^2/2$, where ρ is density and V_p is the particle velocity. This relationship partly carries through to surface waves and reflected waves; Rayleigh's principle states that the total elastic strain energy (integrated over the wave) equals the kinetic energy [e.g., *Bullen and Bolt*, 1985, pp. 302–305].

Seismologists express the attenuation of low-amplitude waves with the quality factor Q. For a monochromatic wave with period T, the elastic and kinetic energies decrease by a factor of $\Delta W/W=Q^{-1}$ over a time of T/π, where ΔW is the energy lost in one half-cycle [e.g., *Kjartansson*, 1979; *Bullen and Bolt*, 1985, p. 101]. For a linearly attenuating material, this factor does not depend on the amplitude of the wave.

Nonlinear attenuation occurs at higher dynamic stresses that exceed the elastic limit of the material. Anelastic strain produces unrecoverable deformation of the material; the rate of the anelastic strain is a function of

the dynamic stress, $\varepsilon'(\tau)$. The instantaneous rate of dissipation from anelastic deformation is then $W'=\varepsilon'(\tau)\tau$. Attenuation, the net diminution of energy over a wave cycle, then is directly related to the anelastic strain over the cycle in this model. The rate of attenuation varies nonlinearly with wave amplitude when ε' increases rapidly with dynamic stress. One recovers linear attenuation for $\varepsilon' \propto \tau$; then $W' \propto W$.

We note that the behavior of attenuation in the frequency domain differs between linear and nonlinear attenuation. For linear attenuation, the signal may be mathematically represented in the frequency domain by a linear Fourier integral. High-frequency signal dies off faster than lower frequency signal. Nonlinear attenuation cannot be represented in this manner; its effects are not the same as increasing linear Q^{-1} at high amplitudes.

We concentrate on nonlinear attenuation within rock at ~10 to a few hundred meters depth. We consider that the rock fails by cracking in friction. Individual cracking events sometimes generate brief pulses of high-frequency energy [*Fischer et al*., 2008a, 2008b; *Fischer and Sammis*, 2009]. The strain rate $\varepsilon'(\tau)$ is quite small when the dynamic stress is too feeble to cause failure and quite high when the dynamic stress approaches the frictional failure criterion. Cracking only mildly decreases the shear modulus G in our formulation and we treat G as constant. We do not consider loose soils for which a large literature exists [e.g., *Hartzell et al*., 2004]. Soil failure may greatly decrease the shear modulus [*Assimaki et al*., 2011]. Neither do we consider liquefaction occurs in unconsolidated materials when shaking causes collapse of the pore space.

Still the form of the anelastic strain rate function $\varepsilon'(\tau)$ is not well defined especially when dynamic stress changes the mean stress within the rock mass $-\sigma_{ii}/3$, where σ is the full stress tensor (compression negative). With regard to theory, we examine plausible simple relationships for $\varepsilon'(\tau)$. We make the reasonable and testable assumption that rocks do not distinguish among dynamic stresses from different classes of waves. For reference, *Roten et al*. [2014] made this assumption in their three-dimensional numerical calculations on strong seismic waves from San Andreas events. In addition, long-term tectonic strains produce ambient stresses within rock masses. *Roten et al*. [2014] included the interaction of these stresses with seismic waves in their southern California models. With regard to data, we present cases where the types of impinging seismic waves are evident upon visual inspection of a single-station record. We retain the traditional wave classes to aid discussion as our data include signals that are essentially *S* waves, *P* waves, Rayleigh waves, and near-field velocity pulses. Analytical theory is then feasible and its predictions are qualitatively simple.

In this study, we first review frictional failure in section 2. Then after section 3, we use records from the 2011 M_w 9.0 Great Tohoku earthquake to look for interaction of ~3 s Rayleigh waves with ambient tectonic stress and to look for interaction of these Rayleigh waves with high-frequency *S* waves. We briefly examine a record from the 2008 M_w 6.9 Iwate-Miyagi earthquake for interaction of high-frequency *P* waves with high-frequency *S* waves. We examine an older record of the 1992 M_w 7.3 Landers main shock for interaction of high-frequency *S* waves with the near-field velocity pulse.

2. Frictional Failure Theories

We examine cases where nonlinear attenuation likely occurs from frictional failure within rock, reviewing basic theories for individual slip planes and for stress invariants. We then consider time-dependent friction for the purpose of qualitatively integrating the behavior of many fractures to obtain predictions on the net behavior of rock masses. We then consider changes of normal traction (and mean stress), where appropriate predictions are less evident.

2.1. Mohr Diagram for Rayleigh Wave

We present the theory for optimally oriented fractures with a Rayleigh wave to introduce the failure of an individual fracture. For simplicity, we assume fluid pressure is hydrostatic. The effective lithostatic stress (compression positive) is $P_{\text{eff}}=(\rho-\rho_w)gz$, where ρ is rock density, ρ_w is water density, g is the acceleration of gravity, and z is depth. Figure 1 illustrates the Mohr diagram in which the effective stresses perturb caused by Rayleigh waves. The angle θ on the Mohr diagram is related to the coefficient of friction μ by $\sin(\theta)=\mu/(1+\mu^2)^{1/2}$ [e.g., *Jaeger et al*., 2007, p. 92]. We ignore cohesion as we assume that the shallow rock

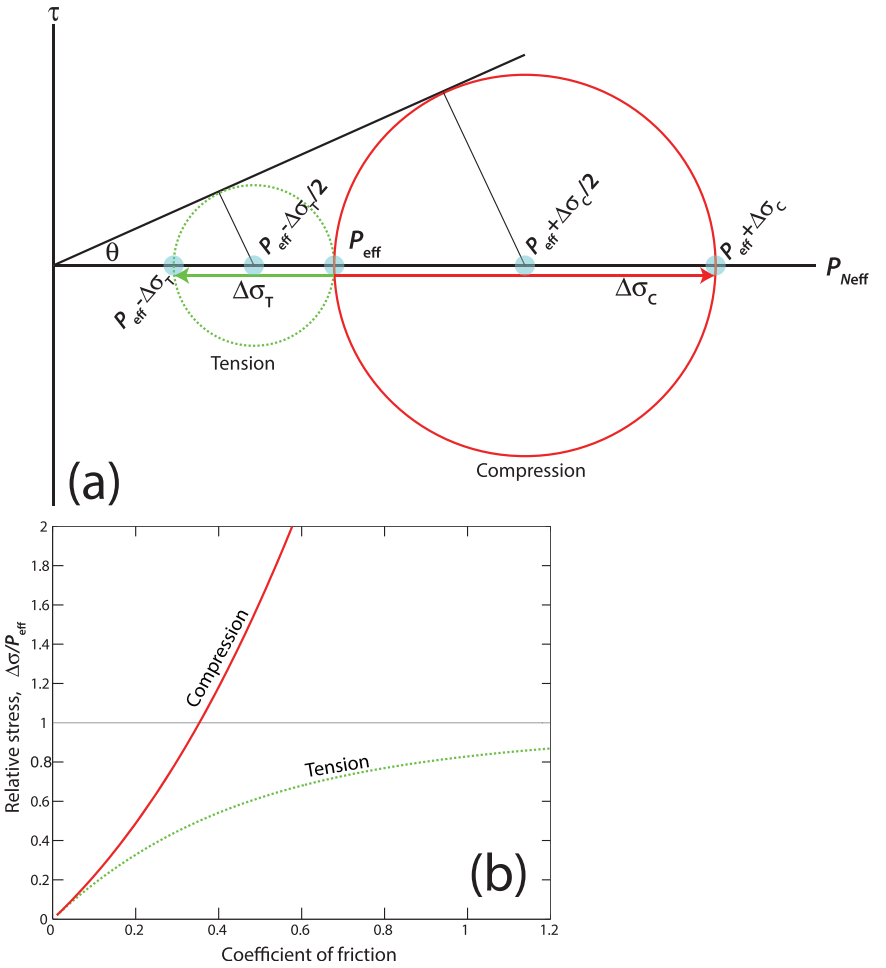

Figure 1. (a) Schematic Mohr diagram for application to Rayleigh waves. The vertical effective stress P_{eff} stays constant at shallow depths. The term P_{Neff} is the effective stress perpendicular to a plane. A smaller change in horizontal stress is needed for shear failure with tension than with compression. (b) The relative stress change for failure as a function of the coefficient of friction.

mass is already pervasively cracked. We also assumed that the pervasive fractures are oriented randomly in all orientations. For a given random stress tensor, some fractures will be well oriented for frictional failure.

We consider shallow depths where rock is present. The vertical principle effective stress is P_{eff} with hydrostatic pressure. Figure 1 shows that the horizontal effective stress differs from the vertical stress by $\Delta\sigma$ (compression positive). We assume for a simple reference case that there is no ambient tectonic stress, equivalently the vertical and horizontal principle stresses are equal before shaking begins. The Rayleigh wave imposes horizontal stresses in its direction of propagation. The horizontal principle effective stress for a symmetrical wave is $P_{eff} \pm \Delta\sigma$, where the plus sign denotes horizontal compression and the minus sign horizontal extension. In general, both dynamic stresses from the Rayleigh wave and ambient tectonic stresses contribute to the difference between horizontal and vertical stress.

Based on the geometry of the Mohr diagram in Figure 1, the stress perturbation for failure is

$$\Delta\sigma_{fail} = \left[\frac{2\mu}{(1+\mu^2)^{1/2} \mp \mu}\right] P_{eff}, \tag{1}$$

where $\Delta\sigma_{fail} = \Delta\sigma_T$ for horizontal tension with the plus sign and $\Delta\sigma_{fail} = \Delta\sigma_C$ for compression (Figure 1). It is obvious that the additional tensional stress for failure is less than the compressive stress. For the tensional case, the bracket in (1) approaches 2μ in the limit $\mu \to 0$ and 1 in the limit $\mu \to \infty$, which is equivalent to failure on opening-mode fractures at zero effective stress.

2.2. Frictional Criteria for Rock Mass

It is likely that a large network of interacting fractures exists within rock masses when the shear modulus G is much less than that of intact rock. We treat the rock mass as a continuum. Qualitatively, fractures accommodate much of the macroscopic strain by dilation, closure, and shear slip. The local traction on a fracture differs from that associated with the macroscopic stress. For example, elastic (and anelastic) slip on a fracture imparts stress on nearby fractures including those with different orientations. Then macroscopic horizontal shear stress and macroscopic horizontal extensional and compressional stresses may modify tractions on the same small fracture. Macroscopic stresses thus may interact nonlinearly.

The well-known *Drucker and Prager* [1952] plastically theory is an obvious candidate to represent the cracked rock masses with stress invariants. For example, *Roten et al.* [2014] used this rheological construct in nonlinear models of wave propagation from San Andreas Fault events near Los Angeles. In the absence of cohesion, friction failure occurs when $|\tau| > \mu_{\text{start}}|P|$, where $|\tau| \propto \sqrt{\tau_{ij}\tau_{ij}}$ is the second invariant of normalized deviatoric stress so that it is the shear traction in simple shear and $|P| \equiv -\sigma_{ii}/3$ (compression negative in σ) is the mean compressive stress. The elastic deviatoric strain energy is proportional to $\tau_{ij}\tau_{ij}$. As a caveat, failure theories based on invariants do not adequately represent opening-mode fractures when the mean stress is compressive and when one of the principle stresses is into or near tension [*Jana and Chatterjee*, 2013].

Drucker and Prager [1952] plasticity has the same qualitative implication as the Mohr diagram for Rayleigh waves (Figure 1). The rock is closer to failure from horizontal tension than from horizontal compression. However, the formalism does not yield exactly the same failure predictions as the Mohr diagram. For example, the principle stresses for plane strain at shallow depths for a Rayleigh wave propagating in the x direction are $P_{zz}=P_{\text{eff}}$, $P_{xx}=P_{\text{eff}}\pm\Delta\sigma$, and $P_{yy}=P_{\text{eff}}\pm\nu\Delta\sigma$, where ν is Poisson's ratio. The second invariant is $|\tau|=\text{sqrt}((1-\nu+\nu^2)/3)\Delta\sigma$. The pressure invariant is then $|P|=P_{\text{eff}}\pm\Delta\sigma(1+\nu)/3$. The failure criterion is thus

$$\mu_{\text{start}}=\frac{\Delta\sigma\sqrt{(1-\nu+\nu^2)/3}}{P_{\text{eff}}\pm\Delta\sigma(1+\nu)/3}. \tag{2}$$

The horizontal stress change to cause failure becomes singular in horizontal compression for sufficiently large μ_{start}.

2.3. Time-Dependent Friction

Seismic waves suddenly impose dynamic stresses on rocks that have been at rest for a long time. Qualitatively, the starting coefficient of friction on fractures that have been idle for a long time is higher than the sliding coefficient of friction once the fracture has failed. *Dieterich* [1979] and *Ruina* [1983] developed rate and state friction formalism to represent the dependence on frictional strength on the history of a fracture.

We begin with the obvious extension rate and state formalism on sliding surfaces to *Drucker and Prager* [1952] plasticity. We use the notation of *Sleep and Hagin* [2008] and *Sleep and Erickson* [2014], who applied rate and state friction to rock damage and nonlinear attenuation by dynamic stresses from strong seismic waves. We begin with the behavior on one small fracture with the intent of considering the cumulative effects of numerous such fractures with a rock mass. The instantaneous shear traction on our fracture is

$$\tau=P[\mu_0+a\ln(V/V_{\text{ref}})+b\ln(\psi/\psi_{\text{norm}})], \tag{3a}$$

where the dominant term $\mu_0 \approx \tau/P$ represents the approximation that the coefficient of friction has a constant value for a given surface (Amontons' law), a and b are small ($\sim$0.01) dimensionless constants, V is the sliding velocity, and V_{ref} is the reference velocity. The state variable ψ includes the effects of healing and damage. We consider its evolution over time later in this subsection. The factor ψ_{norm} is the normalizing value of the state variable, which represents transient variations of normal traction on fractures and here changes in mean stress [*Linker and Dieterich*, 1992]. Note that $\mu_0-a\ln(V_{\text{ref}})$ is effectively one material constant; V_{ref} can be set to a convenient value, for example, where deformation would relax the shear traction over the half period of the seismic wave.

We generalize (3a) to represent effective value of the anelastic deviatoric strain rate tensor ε'_{ij} within a rock mass where numerous small fractures slip. A simple modification to apply (3a) is to replace the shear traction τ with shear invariant $|\tau|$ and the normal traction P with the pressure invariant $|P|$. For brevity, we

assume that the small fractures have random orientations, which leads to an isotropic rock mass. The deviatoric stress within the rock mass in terms of invariants is

$$|\tau| = |P|[\mu_0 + a\ln(|\varepsilon'|/\varepsilon'_{\text{ref}}) + b\ln(\psi/\psi_{\text{norm}})], \tag{3b}$$

where $|\varepsilon'| \propto \sqrt{\varepsilon'_{ij}\varepsilon'_{ij}}$ is the deviatoric strain rate invariant (it is here normalized so that it is strain rate in simple shear) and $\varepsilon'_{\text{ref}}$ is a reference strain rate. Rewriting (3b) yields a trial flow law for a rock mass,

$$\varepsilon'_{ij} = \varepsilon'_{\text{ref}}\left[\frac{\tau_{\text{ij}}}{|\tau|}\right]\exp\left[\frac{|\tau| - \mu_0|P|}{a|P|}\right]\left[\frac{\psi^{-b/a}}{\psi^{-b/a}_{\text{norm}}}\right], \tag{4}$$

where ψ is the value the state variable on fractures within the rock mass. Here we use the relationship $\varepsilon'_{ij}/|\varepsilon| = \tau_{ij}/|\tau|$ to include the directionality of the strain rate. The first bracket represents the inference that anelastic deviatoric deformation has the sense to relax the applied deviatoric stress. The exponential term indicates that the strain rate increases from immeasurably slow to exceedingly fast over a small change in stress as $a \approx 0.01$ and $|\tau|/|P| \approx 1$. We show that the existence of a network of individual fractures within rock masses makes this property unlikely. To discuss the fate of these individual fractures, we let V_{ref} be the velocity that relieves the shear traction over the duration time of the dynamic stress. The starting coefficient of friction on a fracture is from (3a) then

$$\mu_{\text{start}} \approx \mu_0 + b\ln(\psi/\psi_{\text{norm}}). \tag{5}$$

The net behavior of the rock mass results from the combined sliding of numerous fractures. We examine this feature by considering the sliding velocity form of (4) on an individual fracture from (3a),

$$V = V_{\text{ref}}\exp\left[\frac{\tau - \mu_0 P}{aP}\right]\left[\frac{\psi^{-b/a}_{\text{start}}}{\psi^{-b/a}_{\text{norm}}}\right], \tag{6}$$

where ψ_{start} is the value of the state variable on our fracture at the start of shaking. Qualitatively, the anelastic strain rate and nonlinear attenuation are expected to increase gradually with the dynamic stress of the impinging wave rather than over a sharp jump in (6) with a well defined starting coefficient of friction in (5). Specific processes include for avoiding the sharp jump of the sliding velocity: (1) The state variable differs between fractures. The starting coefficient of friction in equation (6) thus varies. The parameter μ_0 may also vary between fractures. (2) Past slip on numerous fractures leaves (somewhat random) residual stresses that are prestresses for the next strong shaking. Favorable stressed fractures thus fail under macroscopic dynamic stresses that are too low to cause frictional failure on unstressed fractures in equation (5). (3) The local tractions on fractures differ from the values predicted from the macroscopic stress. Fractures with high shear tractions and low normal tractions fail first.

We continue with the construct of rate and state friction to qualitatively constrain the value of the state variable in (6) for individual fractures and its effective value for the rock mass in (4). In general, the state variable in (6) represents the history of one fracture. The aging law [*Dieterich*, 1979] represents behavior when the fracture is at rest during earthquakes and also behavior after sudden increases in normal traction

$$\frac{\partial\psi}{\partial t} = \frac{V_{\text{ref}}P^{\alpha/b}}{D_{\text{age}}P^{\alpha/b}_{\text{ref}}} - \frac{\psi V}{D_{\text{age}}}, \tag{7}$$

where t is time, D_{age} is the slip to significantly change the state variable. The pressure term represents the effect of sudden changes in normal traction; $\alpha \approx 0.2$ (the experimental value of *Linker and Dieterich* [1992]) is a positive dimensionless coefficient, and P_{ref} is a reference normal traction. The state variable increases with linearly time on fractures that are not currently sliding, $V \approx 0$ (i.e., healing).

The slip law [*Ruina*, 1983] represents actively sliding fractures,

$$\frac{\partial\psi}{\partial t} = -\frac{V\psi}{D_{\text{slip}}}\ln\left[\frac{P^{\alpha/b}_{\text{ref}}V\psi}{P^{\alpha/b}V_{\text{ref}}}\right], \tag{8}$$

where D_{slip} is the slip to significantly change the state variable. The steady state value of the state variable in (8) when sliding is occurring is

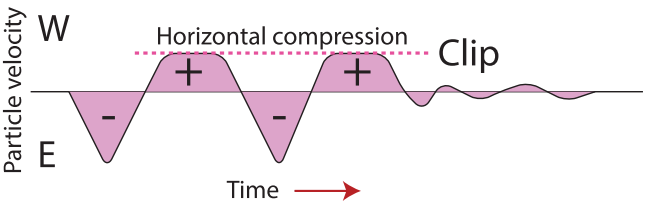

Figure 2. Schematic diagram of arriving Rayleigh wave where nonlinear attenuation clipped half cycles in one direction. Westward traveling waves would clip on west half cycle if shallow strong fault-normal compression existed in the Tohoku region. The mean velocity is still zero in the far field where there is no static displacement.

$$\psi_{ss}=\frac{P^{\alpha/b}V_{\mathrm{ref}}}{P_{\mathrm{ref}}^{\alpha/b}V}. \tag{9}$$

The coefficient of friction at steady state sliding from (8) is independent of normal traction when $\psi_{\mathrm{norm}}=(P/P_{\mathrm{ref}})^{\alpha/b}$.

We begin with the state of a rock mass before shaking starts. The state variable from (7) of individual fractures depends linearly on the time since the fracture lastly slipped, and the state variable in (9) became quite small during sliding. The weakest fractures would have failed during the most recent episode of strong shaking. The state variable on a slipping fracture decreases rapidly toward the steady state value in (9), which greatly weakens the fracture. The net effect of (5) and (9) is that an individual fracture either fails or stays intact. At shallow depths, a failed fracture in the irregular local stress field may come into opening tension and have near-total stress drop. To confirm the reality of sudden failure caused by the stress drop, dynamic strain in the shallow subsurface drives small earthquakes [*Fischer et al.*, 2008a, 2008b; *Fischer and Sammis*, 2009]. The largest of these events produce accelerations above 1 g [*Aoi et al.*, 2008; *Sleep and Ma*, 2008]. Failed fractures strengthen with time following the aging law in (7) but remain weaker than intact aged fractures during hiatuses in shaking. The range of the state variable in (4) between intact and failed fractures thus becomes large once the rock mass begins to dynamically fail in friction. The range of the coefficient of friction of fractures in (5) thus increases.

This behavior of a fracture that is suddenly loaded by large dynamic stresses differs from the behavior of a slowly loaded creeping fracture. In the former case, the shear traction on the fracture will increase until the slip velocity in (6) becomes large enough to relieve the shear traction buildup. Once slip is under way, the state variable decreases in (8) further weakening the fracture. The slip velocity may well increase to the level that inertia is important, thereby generating seismic waves. The exact values of the parameters a and b are not important. In contrast, equations (2) and (9) yield the well-known behavior of a surface at steady state sliding. The steady state shear stress is $\tau_{ss}=P[\mu_0+(a-b)\ln(V/V_{\mathrm{ref}})]$. This shear traction increases with sliding velocity if $a>b$. Steady state shear traction decreases with sliding velocity if $a<b$. Steady state sliding is then unstable if the system loading the fracture is sufficiently elastically compliant. For reference, the laboratory value of $a-b$ in shale is -0.0032 to 0.009 [*Kohli and Zoback*, 2013].

An equation of the general form of (4) thus may be appropriate for a rock mass. The predicted strain rate at the start of failure is,

$$\varepsilon'_{ij}=\varepsilon'_{\mathrm{ref}}\left[\frac{\tau_{\mathrm{ij}}}{|\tau|}\right]F\left\{\left[\frac{|\tau|-\mu_0|P|}{a|P|}\right]\right\}\left[\frac{\psi^{-b/a}}{\psi_{\mathrm{norm}}^{-b/a}}\right], \tag{10}$$

where anelastic strain is still in the orientation to relax the deviatoric stress. The stress invariants and the past history of the rock mass are still relevant. The final bracket the state variable is involved, although some fractures fail before others. That is, the effective value of ψ decreases as the rock mass becomes anelastic. The function F in (10) is thus more mild than the exponential in (4). The failure strain rate is low but not zero at modest shear tractions and given mean stress. The strain rate becomes quite large at high $|\tau|/|P|$; greater values of $|\tau|/|P|$ cannot be reached with reasonable seismic waves. This effect clips the amplitude of the attenuated waves (Figure 2).

2.4. Application to Failure of Horizontal Fractures From Vertical *S* Wave

With forethought to our data, we consider the specific case where low-frequency Rayleigh waves nonlinearly suppress high-frequency vertically propagating *S* waves to obtain a trial form related to (10). Then the wavelength of the Rayleigh wave is much greater than that of the *S* wave. We consider that there are very many fractures in the rock mass; they are small relative to the wavelengths of the *S* waves. At a given small fracture in the rock, the dynamic stress from the Rayleigh wave changes

slowly with time while the dynamic stress from the *S* wave changes rapidly. As a hypothesis, a fracture that is already slipping from the dynamic stress of the Rayleigh wave will slip more rapidly when dynamic stresses from the *S* wave are favorably aligned. The anelastic deformation associated with slip on fractures along the direction of the traction imposed by the *S* wave rate will attenuate the *S* wave.

It is necessary to consider the orientations of stresses. We make the approximation in (1) and (2) that Rayleigh waves do not change the vertical effective stress, which is appropriate at depths much shallower than the wavelength of the Rayleigh wave. To the first order, *S* waves produce shear failure on horizontal planes. The Rayleigh wave does not change the mean normal and shear tractions on these planes. A very simple theory based on resolved tractions then predicts that the *S* waves will not interact with the Rayleigh waves.

However, interaction is expected within a pervasively cracked material. That is, we assume that the Rayleigh wave produces random zero-mean tractions on individual horizontal fractures by amounts that are proportional to its dynamic horizontal stress $\Delta\sigma$. The fractures where the Rayleigh wave decreases the normal traction and the fractures where its shear traction aligns with the shear traction of the *S* wave locally fail, when even the macroscopic normal and shear tractions from the *S* wave alone are insufficient for failure.

We model this effect with stress invariants. The resolved shear traction on horizontal planes from the *S* waves $\tau_{hz} \equiv \sqrt{\tau_{xz}^2+\tau_{yz}^2}$ drives horizontal slip on fractures and distributed horizontal shear strain in the rock mass. A trial expression relevant to vertical *S* waves in analogy with (9) for the anelastic strain rate is,

$$\varepsilon'_{hz}=\varepsilon'_{\mathrm{ref}}\left[\frac{\tau_{hz}}{|\tau|_{\mathrm{eff}}}\right]F\left\{\left[\frac{|\tau|_{\mathrm{eff}}-\mu_0 P_{\mathrm{eff}}}{aP_{\mathrm{eff}}}\right]\right\}\left[\frac{\psi_{\mathrm{start}}^{-b/a}}{\psi_{\mathrm{norm}}^{-\mathrm{b/a}}}\right], \tag{11}$$

where slip is in the direction of the resolved shear traction and ψ_{start} indicates that the state variable at the start of shaking is relevant for the initial failure of distributed fractures. A trial form for the effective shear traction term $|\tau|_{\mathrm{eff}}$ is

$$|\tau|_{\mathrm{eff}}^2=\tau_{zh}^2+C^2\Delta\sigma^2, \tag{12}$$

where the first term is square of the shear traction from the *S* waves resolved on a horizontal plane, and the second term is the shear traction caused by the Rayleigh wave as we discussed in (2) with $C^2=(1-\nu+\nu^2)/3$.

2.5. Sudden Changes in Normal Traction and Mean Stress

All seismic waves change the normal traction on individual fractures. *P* waves and Rayleigh waves also change the mean stress. Behavior may be then more complicated than simple friction that depends only on the instantaneous ratio of shear to normal traction as shown in (3a).

We discuss the formalism for individual fractures. The flow law (6) becomes

$$V=V_0\exp\left[\frac{\tau-\mu_0 P}{aP}\right]\left[\frac{\psi^{-b/a}P_{\mathrm{ref}}^{-\alpha/a}}{P^{-\alpha/a}}\right]. \tag{13}$$

Differentiating (13) (as $\partial\tau/\partial P$) at constant sliding velocity and constant state yields the instantaneous change in the apparent coefficient of friction,

$$\mu_{\mathrm{dif}}\equiv\frac{\partial\tau}{\partial P}=\frac{\tau}{P}-\alpha\equiv\mu_{\mathrm{old}}-\alpha, \tag{14}$$

where μ_{old} is the previous apparent coefficient of friction. This equation applies to sudden but not instantaneous changes in normal traction on individual fractures. *Perfettini et al.* [2001] showed that shear traction cannot change instantly with normal traction, so the instantaneous value of $\alpha=\mu_{\mathrm{old}}$ and $\mu_{\mathrm{dif}}=0$. Otherwise, application of (13) results ill-posed physical problems when the fault plane separates dissimilar materials.

A further complication with regard to pressure changes involves fluid pressure within fractures during dynamic normal traction changes. As in (14), the differential coefficient of friction μ_{dif} is less than the long-term coefficient of friction. Physically, the fluid may not be able to drain from (or into) the fracture during

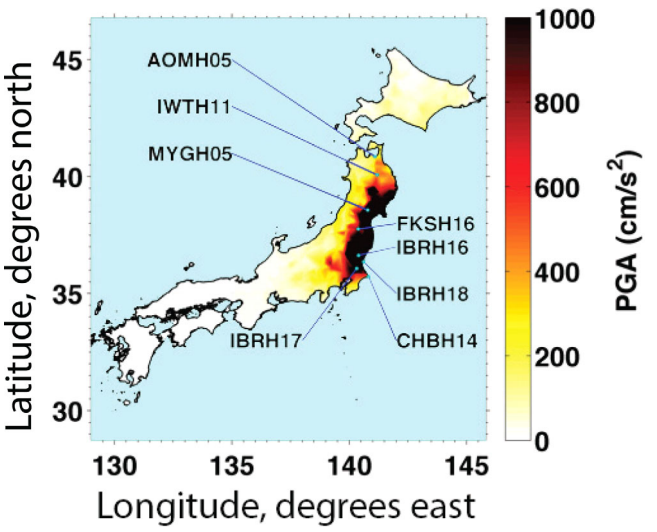

Figure 3. Peak ground acceleration for the Great Tohoku earthquake estimated from KiK-net stations. Collocated surface and borehole stations are discussed in the text.

brief normal traction changes. Then dynamic compression increases the fluid pressure and decreases the effective normal traction. Skempton's coefficient B_s where $\mu_{dif}=\mu(1-B_s)$ represents this effect [e.g., *Wang et al.*, 2014]. Studies of the correlation of aftershocks sequences with dynamic stress changes resolve μ_{dif} to some extent [*Wang et al.*, 2014]. These aftershock data were gathered from events at times of hours to months after the static stress change. The value of μ_{dif} may well be closer to zero for the ~1 s period of our dynamic stress changes over which pore fluid has little time to flow. The effective value of μ_{dif} for changes of mean stress in a rock mass may hence be much less than the typical coefficient of friction. We thus seek field situations where dynamic mean stress changes over the period of a seismic wave.

3. Interaction of Raleigh Waves With Ambient Tectonic Stress

Rayleigh waves provide a case where the dynamic normal traction on fractures and the dynamic mean stress change over the period of the wave. In this section, we discuss nonlinear behavior of Rayleigh waves with regard to their interaction with ambient tectonic stress and prepare for discussion of nonlinear suppression of high-frequency *S* waves by Rayleigh waves in section 4.

3.1. Tohoku Seismograms

The 2011 Tohoku main shock produced strong shaking over much of Honshu (Figure 3). Eight collocated surface and borehole KiK-net stations yielded reliable digital records for our analysis (Figure 4). We correct the orientation of all borehole seismograms before processing the data. Visual examination of broadband and filtered records indicates that *S* waves dominated that high-frequency horizontal signal and 3–4 s Rayleigh waves dominated the low-frequency signal. The horizontal particle velocities are similar at the surface and in the borehole at IBRH16 and MYGH05 as expected for long-period Rayleigh waves (Figures 4 and 5).

With regard to examining horizontal seismograms, dynamic stress is proportional to dynamic velocity. We manipulate well-known equations in Appendix A to obtain the relationship between peak ground velocity (PGV) and peak dynamic stress for Rayleigh waves at shallow depth. With regard to the sign of the effect, dynamic velocity in the direction of propagation causes horizontal compression and dynamic velocity against the direction of propagation causes horizontal tension. This kinematic result can be seen by differentiating the kinematic wave equation for motion in the *x*-direction of propagation with $U_x=U(x-ct)$ (where *c* is wave velocity) with respect to time to obtain particle velocity and then with respect to *x* to obtain strain. Positive strain $\partial U_x/\partial x=U'(x-ct)$ and hence tensile stress occur with negative particle velocity $\partial U_x/\partial t=-cU'(x-ct)$.

The Tohoku seismic sources were to the east of our stations, so particle velocities to the west produced dynamic compression. There is no strong asymmetry of particle velocity. Starting with MYGH05 (which had the highest PGV, Table 1), the WNW oscillations were comparable to the ESE ones (Figure 5). The NE oscillation was somewhat larger than the NW one. There was no strong variation of amplitude with polarity at IBRH18 (Figure 6) and CHBH14 (Figure 6). There were single strong excursions to the SE at IBRH16, to the W at FKSH16, and to the NE at IWTH11. The SW excursion was modestly greater than the N and SE excursions at AOMH05. Vagaries in the sources producing the Rayleigh waves and the local interference of various

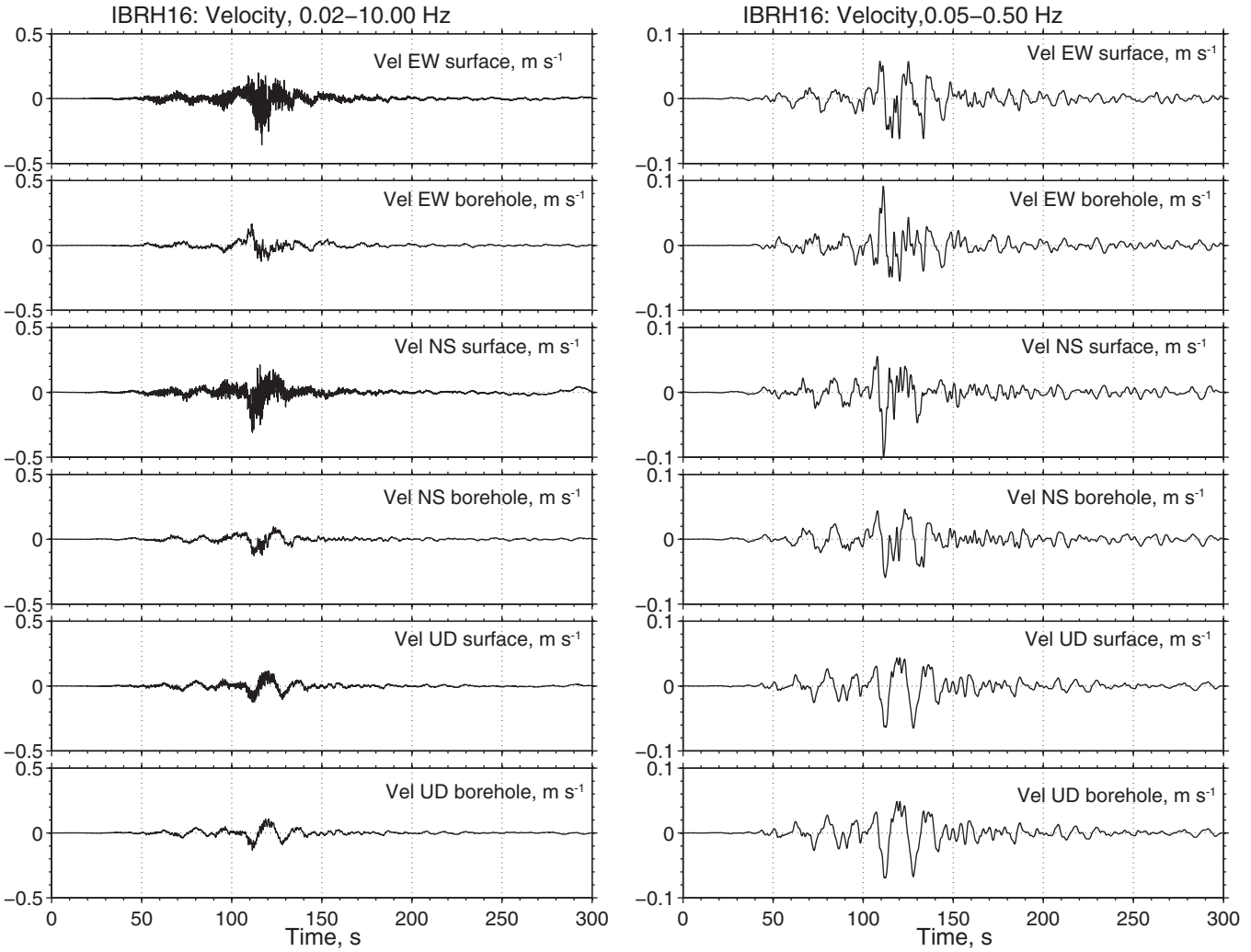

Figure 4. (left) Broadband and (right) filtered particle velocity for station IBRH16. High-frequency shaking is strongest at the surface and on the horizontal components and is thus mostly *S* waves. The low-frequency shaking is similar at the surface and at depth and on all components and is hence mostly Rayleigh waves.

propagating waves at our stations are likely causes of the excursions. There is no consistent direction of strong excursions and not enough excursions for statistical analysis.

3.2. Application of Theory in Absence of Tectonic Stress

We show that our Rayleigh wave data do not show any evident effects of nonlinear attenuation. We discuss the case where ambient tectonic stresses are not important before discussing the case with significant ambient stresses in the next subsection. We obtain the particle velocity necessary for frictional failure on optimal planes in the absence of tectonic stress in Appendix A. The dynamic failure velocity is

$$V_{\text{fail}} = \left(\frac{3B}{8}\right)(g(\rho - \rho_w)z)\left(\frac{c_{\text{Ray}}}{G}\right), \tag{15}$$

where B is a dimensionless coefficient in (A6) related to the coefficient of friction, the second bracket is the hydrostatic effective pressure, c_{Ray} is the Rayleigh wave phase velocity, and G is the shear modulus ($\rho\beta^2$, where β is the shear wave velocity). The constant B is significantly larger for dynamic horizontal compression than for tension.

Strong nonlinear attenuation occurs above a threshold of the particle velocity related to V_{fail}, given formally by (10) where the anelastic strain rate is high. The dynamic stress and the dynamic velocity cannot exceed this threshold. The net effect is that a velocity seismogram will appear clipped at the threshold velocity. In

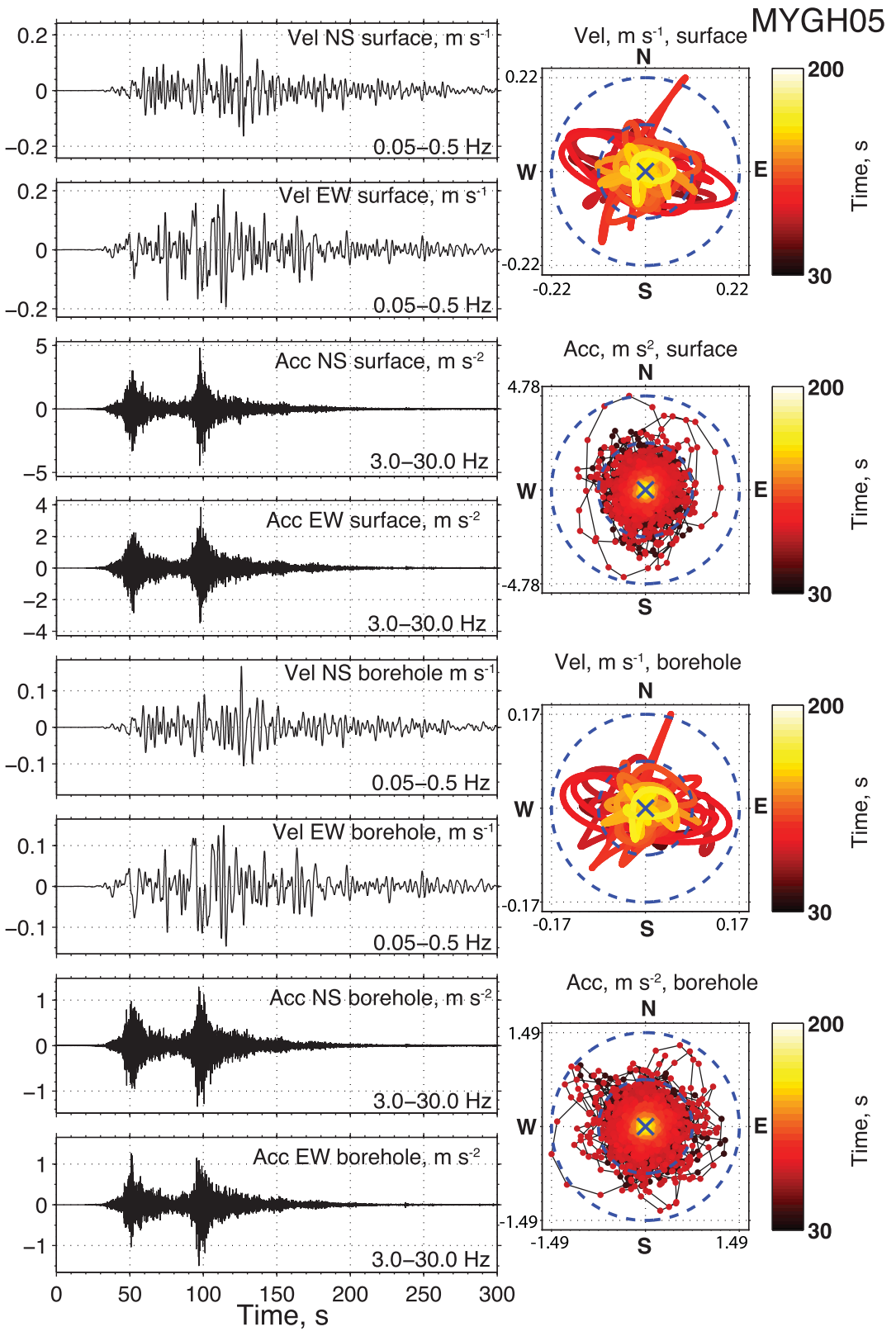

Figure 5. (left) Horizontal acceleration and velocities for paths for station MYGH05. Note that the accelerations are higher at the surface than in the borehole. (right) Horizontal acceleration and velocity paths. There is no obvious asymmetry in largest excursions of the paths.

Table 1. Station Parameters[a]

Station	Lat	Lon	Depth (m)	Rock Type	Period (s)	PGA (m s^{-2})	PGV (m s^{-1})	Velocity Change (%)	Anisotropy Change (%)	ε_{xx}, 10^{-6}
AOMH05	40.8564	141.1033	312	NV	1.56	1.37	0.057	−3.64	40.6	0.02
CHBH14	35.7342	140.823	525	NKS	2.04	1.73	0.065	−1.33	63.4	1.22
FKSH16	37.7643	140.3766	300	QV	1.43	3.54	0.083	−4.02	7.1	19.43
IBRH16	36.6405	140.3976	300	NS	0.87	6.61	0.101	−0.27	55.5	10.21
IBRH17	36.0864	140.314	510	QS	3.71	5.03	0.057	−0.16	−9.3	3.05
IBRH18	36.3631	140.6198	504	KS	1.32	6.32	0.090	−0.09	30.0	11.02
IWTH11	40.0811	141.1915	300	QV	1.51	1.65	0.076	−0.14	46.1	1.43
MYGH05	38.5793	140.7804	337	NS	2.07	4.90	0.172	−0.02	13.9	25.60

[a]Dominant rock type in borehole. NV: Neogene volcanics; NKS, Neogene and Cretaceous sediments; QV, Quaternary volcanics; NS, Neogene sediments; KS, Cretaceous sediments. PGA, broadband horizontal peak ground acceleration measured at surface; PGV, filtered (0.05–0.5 Hz) horizontal peak ground velocity measured at surface. Negative velocity change: the *S* wave velocity decreased after shaking [*Nakata and Snieder*, 2011]. Negative anisotropy change: the material became less anisotropic after shaking [*Nakata and Snieder*, 2012b]. ε_{xx}: east-west longitudinal strains computed by K. Johnson (personal communication, 2014) from model of *Simons et al.* [2011], extension positive.

the absence of tectonic stress, a symmetrical Rayleigh wave will produce failure during the tensile half cycle without producing failure on the compressive half-cycle if the Mohr diagram in fact applies at the seismic frequency (Figure 2). The waveform will clip on the tensile cycle rather than on the compressive cycle. In the case of our data, eastward particle velocities would be suppressed. We did not detect that effect. This means that the observed Rayleigh-wave particle velocities at our stations were somewhat below V_{fail} in (15) for pervasive frictional failure in the upper few hundred meters that would have strongly attenuated our Rayleigh waves.

To briefly digress, this expected asymmetric material response and hence asymmetric clipping in Figure 2 is kinematically similar to that of *P* waves as we discuss later [*Yamada et al.*, 2009; *Tobita et al.*, 2010; *Kinoshita*, 2011; *Bradley and Cubrinovski*, 2011]. The ratio of dynamic normal traction to lithostatic pressure then scales to the vertical dynamic acceleration normalized to the acceleration of gravity (Appendix B). Shallow rock has little strength in tension; dynamic acceleration clips at −1 g in free fall. The dynamic acceleration during the compressive part of the cycle may reach large (>>1 g) values, as rock resists crushing from vertical compression.

Returning to the data, we provide simple example calculations for V_{fail} and Love wave failure velocities from (A8) for comparison with the sites of our stations. Rock and water densities are 2500 and 1000 kg m^{-3}, respectively. The coefficient of friction by assumption is μ=0.8. The factor *B* in horizontal tension in (A7) is then 0.77. The ambient *S* wave velocity for exhumed sediments at IBRH16, IBRH18, and CHBH14 (Figure 6) is 2000 m s^{-1} from 100 to 300 m depth. The phase velocities of 3–4 s Rayleigh waves and Love waves are 3000 and 3200 m s^{-1}, respectively [*Nishida et al.*, 2008]. The Rayleigh particle velocity for failure at 300 m depth is 0.38 m s^{-1} and the Love wave failure velocity is 1.13 m s^{-1}. The Rayleigh wave failure velocity at 100 m depth is 0.13 m s^{-1}. The failure velocities are 4 times the values at IBRH16, MYGH05, FKSH16, IWTH11, and AOMH05, where the *S* wave velocity from 100 to 300 m depth is ∼1000 m s^{-1}. Observed PGV was much smaller than the expected failure velocities at all stations (Table 1).

Note that nonlinear attenuation may occur along the full path of the Rayleigh wave. In this case, the eastward tensile cycle of Rayleigh waves might have been suppressed before the waves reached our stations. The waveform of Rayleigh waves in our area is retained during their propagation as the group and phase velocities depend weakly on frequency [*Nishida et al.*, 2008].

3.3. Dynamic Failure With Regional Horizontal Compression

It is conceivable that the ambient tectonic stresses were compressive enough that the modest dynamic stresses brought the rock into compressional failure. In our case, this effect would preferentially suppress westward particle motions, although we did not obviously observe this effect.

To review tectonics, the area with our stations has active NS striking thrust faults and is thus crudely in east-west compression [*Headquarters for Earthquake Research Promotion*, 2011]. Analysis of crustal earthquake mechanisms indicates that EW compression within the area of our station existed before the main shock and that static stress changes from the main shock modified and partly reoriented the crustal stress [*Simons*

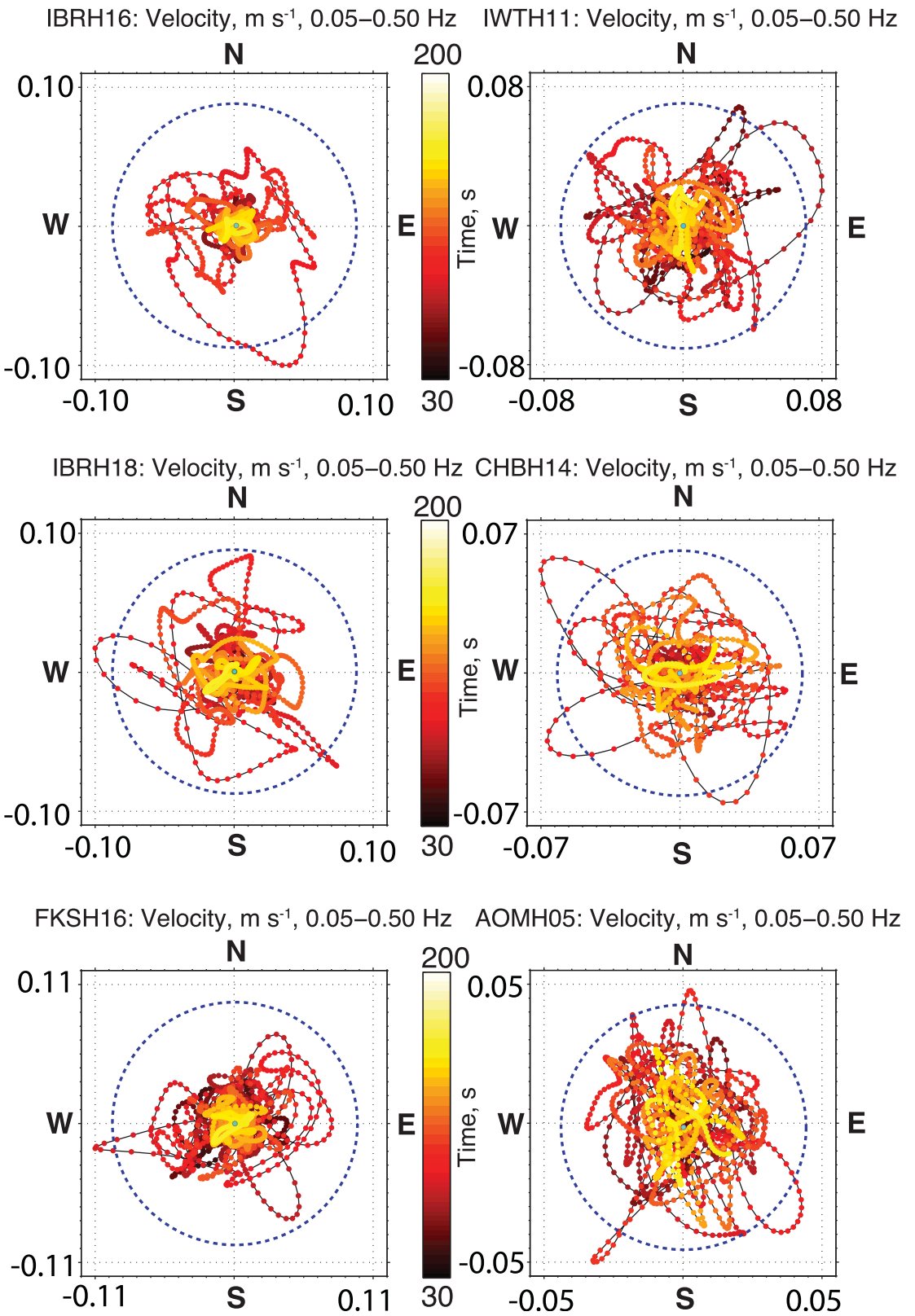

Figure 6. Horizontal velocity paths for surface stations IBRH16, IBRH18, FKSH16, IWTH11, CHBH14, and AOMH05 as in Figure 5. There is again no obvious asymmetry of large excursions.

et al., 2011; *Toda et al*., 2011; *Hasegawa et al*., 2012; *Yoshida et al*., 2012; *Yang et al*., 2013]. *S* wave splitting experiments indicate that this stress existed at the depths of the boreholes [*Nakata and Snieder*, 2012a,b]. No stress measurements, however, are available at the few hundred meter depths of our boreholes. Such stress-orientation measurements are typically taken below 1 km depth [*Townend and Zoback*, 2000; *Zoback and Townend*, 2001; *Zoback et al*., 2002].

With regard to negative result that no effect of tectonic stress on Rayleigh waves was detected, previous events may have self-organized the subsurface so that typical shaking causes pervasive frictional failure. We consider the shear-modulus and the ambient tectonic stress.

First, the shear modulus in (15) may have self-organized over several earthquake cycles so that it increases linearly with depth [*Sleep*, 2011, 2014; *Sleep and Erickson*, 2014]. For an example, we start with intact rock all the way to the surface and consider failure during the tensional cycle of ground motions. Rayleigh waves with maximum particle velocity of V_{past} given by previous events impinged on the region. From (15), V_{fail} was small within intact shallow rocks with large G. Failure occurred downward to the depth where $V_{\text{past}}=V_{\text{fail}}$ for the stiffness G_{int} of intact rocks. Frictional failure from repeated events caused cracking that reduced the stiffness so that $V_{\text{past}} \approx V_{\text{fail}}$ above that depth. In subsequent events, the rock barely reached frictional failure under the imposed strain $V_{\text{past}}/c_{\text{Ray}}$ of typical strong shaking. This process, called low-cycle fatigue, occurs in engineering applications where a brittle part experiences oscillating strain boundary conditions [*Lubliner*, 1990].

With regard to observations, the present *S* wave velocity increases approximately with the square root of depth if the shear modulus increases linearly (Figure 7). This situation has been observed in seismically active regions [*Sleep*, 2011, 2014; *Sleep and Erickson*, 2014]. The rock in the boreholes (other than IBRH17) consists of exhumed volcanic and/or sedimentary rocks that likely meet the criterion for having been likely initially stiff. Retaining $\rho=$ 2500 kg m^{-3}, $\rho_w=$ 1000 kg m^{-3}, and μ=0.8, we estimate past PGV between 0.45 and 1.04 m s^{-1} from (15), which is greater than the observed PGV from the Tohoku event.

In addition, anelastic strain as in (10) occurs with the sense to relax the total dynamic and ambient stress. There is a tendency for repeated strong shaking to relax ambient tectonic stress away from frictional failure [*Sleep*, 2014]. For an example, we start with our shallow rocks near compressive frictional failure in the thrust-faulting regime. Failure occurs preferentially where the dynamic stress and the static stress are favorably oriented. The overall anelastic strain within the rock mass systematically reduces the ambient stress in each event and this strain accommodates the long-term tectonic horizontal convergence. Deeper compression then gradually reloads the shallow stress. The typical ambient stress will be less than that for frictional failure if the deep process is slow and strong shaking is frequent.

3.4. Effect of Static Stress Changes

We consider show that static stress changes at our stations were likely modest at our borehole depths even though these stations are within the near field. For example, the static horizontal strain at MYGH05 is $\sim$25.6 $\times$ 10^{-6} (Table 1). The *S* wave velocity deep in the hole is $\sim$1000 m s^{-1} so the shear modulus is $\sim$2.5 GPa and the stress change is $\sim$0.17 MPa. For reference, the failure stress in extension in (14) is 1.1 MPa at 100 m depth and 3.4 MPa at 300 m depth. The static strain at IBRH16 and IBRH18 is $\sim$10^{-5} and the deep *S* wave velocity is $\sim$2000 m s^{-1}, and hence the static stress change is 0.27 MPa. For comparison, the PGV of 0.172 m s^{-1} at MYGH05 produced a longitudinal strain of $\sim$6 $\times$ 10^{-5}.

So static stress from coseismic strains did not likely to dominate nonlinear attenuation of Rayleigh waves in our data. They were, however, not negligible. Part of the change in the *S* wave velocity observed within boreholes in the region may be associated with changes in ambient stress [*Minato et al*., 2012].

4. Suppression of High-Frequency *S* Waves by Low-Frequency Rayleigh Waves

Strong *S* waves coarrived with strong Rayleigh waves at our stations (Figure 4). These data provide an opportunity to examine frictional behavior predicted in the trial model in (11) and (12). We are concerned whether the deviatoric stress parameter $|\tau|_{\text{eff}}$ became large enough that nonlinear behavior occurred on horizontal fractures.

The earthquake source was spatially distributed over the fault plane and temporally distributed over the duration of rupture [e.g., *Frankel*, 2013]. Strong body waves and surface waves thus arrived together from

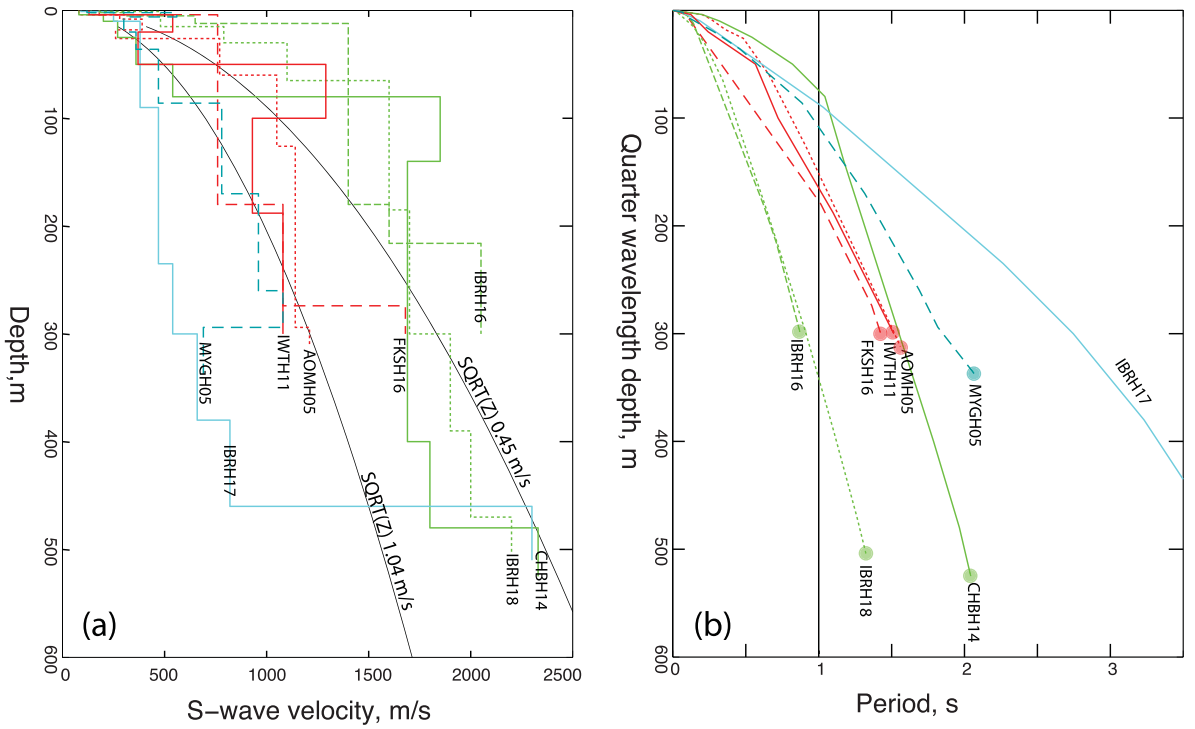

Figure 7. (a) The *S* wave velocity as a function of depth. Curves are piecewise constant. The borehole seismometers are at the ends of the deepest segments. Frictional failure occurs at peak ground velocities of 0.45 and 1.04 m s^{-1} along the square root of depth curves for the physical parameters given in the text. There is some tendency for the observed *S* wave velocities to increase with depth in this way. (b) The quarter-wavelength depth as a function of period. Dots indicate borehole station depths.

the distributed sources over an extended interval at a given station. In contrast, *S* waves arrive before Rayleigh waves for lesser events with spatially and temporally compact sources.

In preparation of the discussion of nonlinear attenuation of *S* waves, we briefly review the behavior of shallow *S* waves for the frictional failure. Conveniently, the peak ground acceleration normalized to the acceleration of gravity is proportional to the Coulomb stress ratio at depth (Appendix B). Frictional failure from *S* waves alone is expected when the normalized PGA exceeds the effective coefficient of friction. Thus, the observed normalized acceleration in should not exceed the effective coefficient of friction in the shallow subsurface,

$$\frac{A_{\mathrm{obs}}}{g} \leq \mu_{\mathrm{eff}}, \tag{16}$$

where A_{obs} is the observed resolved horizontal acceleration.

4.1. Observed Rock Damage and Nonlinearity

There is evidence from transient changes in seismic velocity that nonlinear material behavior did occur during Tohoku shaking within the rocks above the borehole stations. The energy to open fractures that reduced the shear modulus presumably came from the impinging seismic waves. Qualitatively, this rock failure thus was associated with nonlinear attenuation of the wave, but we do not have a good method to predict attenuation from the observed changes in seismic velocity.

We review observation of rock damage as a justification for looking for the effects of nonlinear attenuation on the seismic records. *S* waves reverberated within a 12 m thick gravel layer at IBRH16. *Wu and Peng* [2011, 2012] showed that the period of reverberation increased at IBRH16 during strong shaking. The instantaneous decrease in *S* wave velocity from damage correlated with horizontal acceleration as expected from (16). Long-term changes in the resonant frequency indicate that the gravel was damaged and then slowly healed. The measured resonance period before the main shock was ~0.13 s [*Wu and Peng*, 2012]. The period increased during the strong shaking indicating a decreased *S* wave velocity. By 5 months after the main shock, the resonant period had recovered to ~0.14 s, but not all the way to its preevent value.

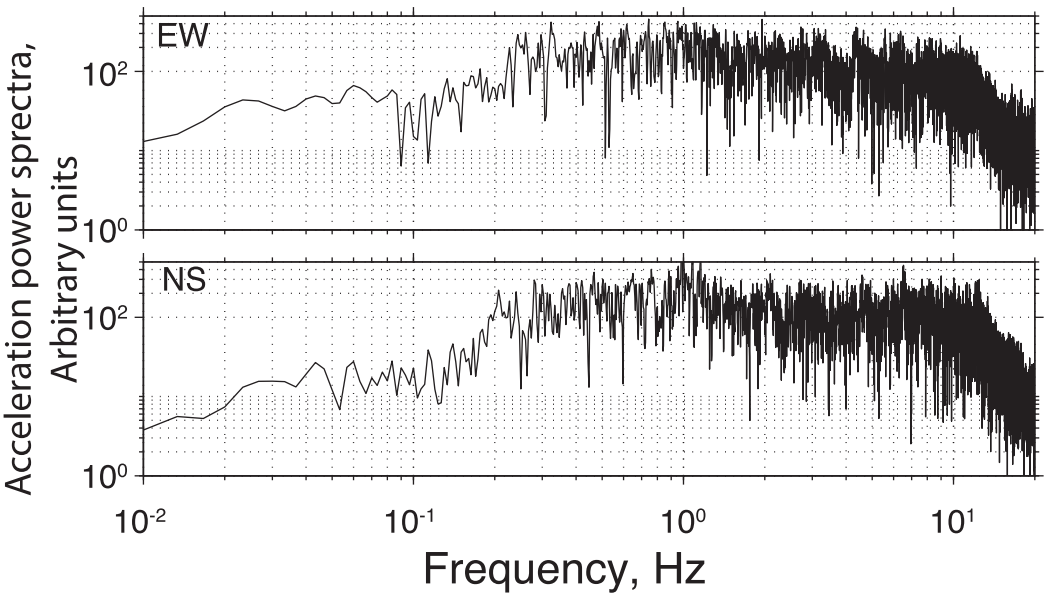

Figure 8. The spectra for the EW and NS surface components of acceleration at station MYGH05 in arbitrary units. Curves are the square roots of the product of the Fourier transform and its complex conjugate. The spectra are relatively flat for frequencies lower than 10–0.5 Hz.

Sawazaki and Snieder [2013] obtained *S* wave velocity changes by correlating signals at the surface and 504 m deep seismographs at IBRH16. They observed similar time-dependent behavior and attributed the travel time changes mainly to *S* wave velocity changes at shallow depths. Similar behavior was observed at other stations (Table 1). *Nakata and Snieder* [2011] obtained *S* wave velocity changes by correlating signals at the surface and 100 m deep seismographs at FKSH18 and *Nakata and Snieder* [2012b] studied records from the 105 m deep borehole and surface stations at FKSH12. The observed *S* wave velocity decreased coseismically and gradually recovered over time. The logarithmic recovery of *S* wave velocity at long times indicates that part of the velocity change was associated with frictional failure as predicted by the aging law (7) [*Nakata and Snieder*, 2011, 2012b; *Sawazaki and Snieder*, 2013].

4.2. Theory of *S* Wave Nonlinear Attenuation in Isolation

We begin by applying (16) considering only *S* waves before discussing their interaction with Rayleigh waves. We estimate the intrinsic coefficient of friction from the observed PGA of ~0.5 g at MYGH05. The surface gravel layer is only 2 m thick at this station and likely had only modest effects on the waveform. The expected reverberation period is ~0.07 s. However, the signal was weak at this frequency (Figure 8). However, there were reverberations associated with the general gradual increase of *S* wave velocity with depth (Figure 8). This borehole penetrated clay-rich exhumed sedimentary rocks.

To obtain an estimate of the intrinsic coefficient of friction of the rock from (B4), we let the shallow rock density be 2500 kg m^{-3} and the water density be 1000 kg m^{-3}. We obtain an intrinsic coefficient of friction of 0.8, which is reasonable of starting friction within somewhat intact clay-rich rock. For comparison, laboratory values of μ for shale range from 0.4 to 0.8 [*Kohli and Zoback*, 2013]. If clipping of normalized acceleration at the effective coefficient of friction in fact occurred, the acceleration is likely to approach its maximum absolute value multiple times. The record at MYGH05 has this property (Figure 5).

For comparison, PGA at IBRH16 and IBRH18 was slightly higher ~0.6 g. *S* waves reverberated within gravel layers beneath these stations. There is 12 m of gravel at IBRH16 and 15 m at IBRH18. The predicted resonance periods are 0.15 and 0.21 s. The measured resonance period before the main shock for IBRH16 was ~0.13 s [*Wu and Peng*, 2012]. Qualitatively, high-frequency signal of about this period dominates the record at IBRH16 (Figure 4). The intrinsic coefficient of friction from (B4) of 1 for these stations applies mainly to the gravel layer. As a general caveat for shallow stations, the assumption that

the water table is at the free surface may be incorrect. For reference, the estimated coefficient of friction is 0.6 (the measured normalized acceleration, not 1, if the water table was below the gravel, setting $\rho_w = 0$ in (B4) for air-filled pores).

4.3. Observed *S* Wave and Rayleigh Wave Interaction

We apply the trial criterion that nonlinear attenuation will become strong when the stress $|\tau|_{\text{eff}}$ in (12) becomes too large. We need to estimate the terms in (12) from the *S* waves and the Rayleigh waves from seismograms.

Starting with acceleration, the *S* wave signal at MYGH05 is high frequency. The spectrum (Figure 8) is broadband, as there is no sharp reflective boundary to produce a sharp resonance (Figure 7). A complication is that deep stresses that cause nonlinear behavior are not fully in phase with the surface acceleration for broadband signal. The relationship in (16) applies approximately to our data (Appendix B), but the seismograph recorded accelerations at the surface while high dynamic stresses and hence nonlinear attenuation occurred around the quarter wavelength depths of the reverberating *S* waves. For example, upgoing and downgoing parts of the complicated signal could constructively interfere at depth without producing an exceptionally high surface acceleration.

The envelope function (the complex absolute value of the Hilbert transform) acts to decrease the phase dependence of plotted acceleration and may be a better indication of the underground stress than raw acceleration for broadband signal. Conveniently, this quantity varies much more slowly with time than do raw accelerations. We use the resolved envelope function, which is the square root of the sum of the squares of the two horizontal envelopes,

$$A_{\text{res}} \equiv \sqrt{A_{\text{NSenv}}^2 + A_{\text{EWenv}}^2}, \tag{17}$$

where A_{NSenv} and A_{EWenv} are the north-south and east-west envelopes.

From Appendix A, the dynamic horizontal stress from the Rayleigh wave is proportional to PGV. We use the resolved horizontal velocity,

$$V_{\text{res}} \equiv \sqrt{V_{\text{NS}}^2 + V_{\text{EW}}^2}, \tag{18}$$

where V_{NS} and V_{EW} are the north-south and east-west velocities, to measure the intensity of the Rayleigh wave. In the data processing, we separate Rayleigh and *S* waves with band-pass filters.

We evaluate frictional failure around the quarter wavelength depth Z_Q. As in (16), the coefficient of friction is expected to bound the observed range of (A_{res}, V_{res}). Applying (12) and (16)–(18) yields the predicted envelope,

$$\left[\frac{|\tau|_{\text{eff}}}{(\rho-\rho_w)gZ_Q}\right] = \left\{\left[\frac{A_{\text{res}}}{g}\right]^2 + \left[\frac{8CGV_{\text{res}}}{3c_{\text{Ray}}(\rho-\rho_w)gZ_Q}\right]^2\right\}^{1/2} < \mu, \tag{19}$$

where the terms are effectively Coulomb stress ratios. The term on the left-hand side is the effective shear stress divided by the effective lithostatic stress. Applying (16) yields the first right-hand bracket associated with *S* waves. Applying (A7) yields in the second bracket associated with Rayleigh wave. The constant *B* in (12) is 0.65 for $\nu = 0.25$. We illustrate its implications of (19) to data by gathering constants and dividing by the coefficient of friction. This yields the normalized equation for an ellipse,

$$\left[\frac{A_{\text{res}}}{A_{max}}\right]^2 + \left[\frac{V_{\text{res}}}{V_{\text{max}}}\right]^2 < 1, \tag{20}$$

where the intercept A_{max} is the maximum amplitude of an *S* wave that can reverberate in the absence of Rayleigh waves and the intercept V_{max} is the Rayleigh particle velocity that brings the shallow material into failure and thus strongly suppresses *S* waves. Our prediction is that observed (A_{res}, V_{res}) values will be bounded by such an ellipse.

We concentrate on data from MYGH05 where the *S* waves reverberated mainly within exhumed sedimentary rocks not gravel. The reverberation occurred mainly within gravel at IBRH16 and IBRH18. The observed

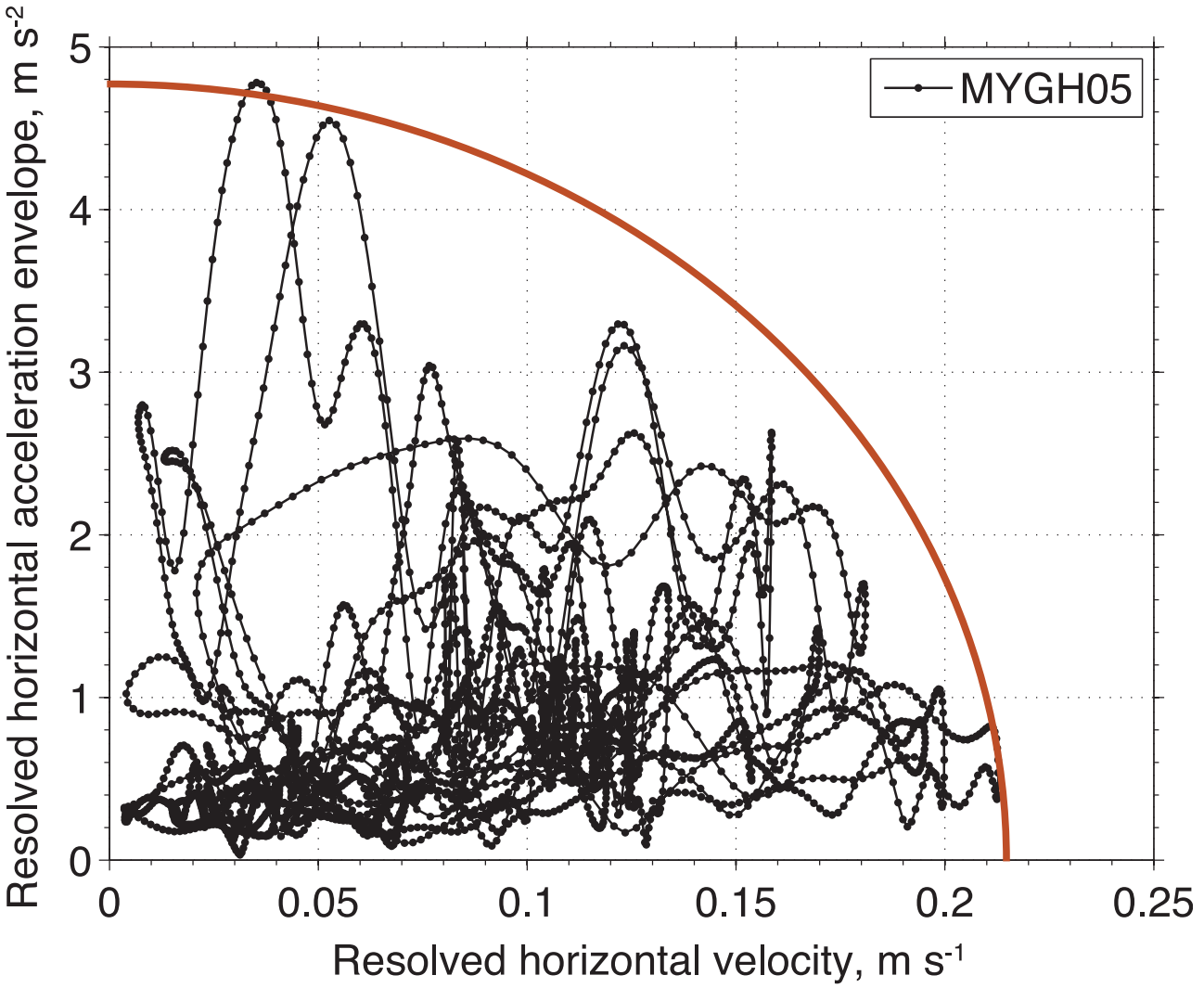

Figure 9. The resolved horizontal acceleration envelope represents dynamic stress at shallow depths from *S* waves at surface station MYGH05. The resolved horizontal velocity represents stress from Rayleigh waves. *S* waves with strong acceleration impinged only when the velocity from Rayleigh waves was low. This behavior is theoretically expected from (20). The sum of the normalized squares of these quantities is proportional to the deviatoric stress invariant. An ellipse is shown for reference.

decrease of shallow *S* wave velocity during strong shaking at these stations [*Wu and Peng*, 2011] may have trapped energy that entered the reverberating layer while its *S* wave velocity was still high and thus increase shaking amplitude [*Assimaki et al*., 2011]. This effect counteracts the diminution of amplitude by nonlinear attenuation.

The data from MYGH05 do lie within an ellipse as predicted by (20) (Figure 9). There are enough data to present example calculations, but not enough to do meaningful statistics. We did not find this behavior at our other Japanese stations. We continue with the MYGH05 to illustrate the procedures from analyzing such data.

The implications of the acceleration intercept ~0.5 g in Figure 9 are straightforward and already discussed in section 4.2. The intercept is a measure of the effective coefficient of friction, 0.5. This would be appropriate if the water table was near the surface.

The implications of the velocity intercept of ~0.215 m s^{-1} are more complicated because nonlinear attenuation occurs over a range of depths, not just at the quarter wavelength depth. We estimate an approximate value for this depth. The power spectrum for MYGH05 drops off above 10 Hz and is flat at somewhat lower frequencies (Figure 8). Much of the energy of the signal resides at frequencies modestly lower than 10 Hz. (The strain energy per volume in the shallow subsurface is proportional to the squares of the plotted

spectra integrated over frequency.) So waves with a period of ~0.1 s are relevant. We let the shallow velocity be ~400 m s^{-1} (Figure 7). The quarter wavelength depth is ~10 m. We retain the phase velocity of 3000 m s^{-1} to estimate the Coulomb stress ratio from the second right-hand bracket of (19) at that depth for the intercept Rayleigh wave particle velocity of ~0.215 m s^{-1}. The Coulomb stress ratio and estimated effective coefficient of friction is 0.4, comparable to 0.5 obtained from the acceleration.

Therefore, the observed intercepts from both dynamic acceleration from high-frequency *S* waves and dynamic velocity from Rayleigh waves are compatible that both wave types brought shallow rock into nonlinear behavior. Figure 9 serves to support the model in (12), (19), and (20) where the average normal traction on horizontal failure planes does not change and where both *S* waves and Rayleigh waves contribute to the shear stress invariant $|\tau_{\text{eff}}|$ for failure.

5. Nonlinear Interaction of *S* Waves With *P* Waves

P waves and *S* waves refract into near-vertical paths in the shallow subsurface. The tensile cycle of *P* waves reduces the normal traction on horizontal planes. Shear slip then should occur on the planes, nonlinearly attenuating *S* waves. That is, strong *P* waves should suppress *S* waves if frictional strength decreases with the instantaneous normal traction. We examine an example involving shallow reverberating waves. The relationship in (16) carries through to *P* waves in that the ratio of dynamic stress to lithostatic stress scales to the vertical normalized acceleration (see Appendix B).

5.1. Observations and Simple Theory

The asymmetry of ground failure from strong *P* waves is well known [*Yamada et al*., 2009; *Tobita et al*., 2010; *Kinoshita*, 2011; *Bradley and Cubrinovski*, 2011]. We illustrate the sign of the effect by considering a shallow (much less than the quarter-wavelength depth) horizontal plane at depth *z*. For simplicity, the free surface exerts no forces. In the static situation, gravity produces a downward force per area of ρgz on the surface. The upward force from lithostatic pressure on the plane of balances this force ρgz. If tensile dynamic stress causes the upward force on the plane to go to zero, shallow rock will accelerate downward in free fall at 1 g. That is, downward accelerations are associated with dynamic tension and upward accelerations with dynamic compression.

If regard to the asymmetry, upward acceleration puts the rock into compression where it is strong. The rock may well remain elastic. Conversely, rock has little strength in absolute tension so the dynamic tension does not drop below ρgz; downward accelerations tend to clip around 1 g where the normal traction becomes zero. In addition, strong dynamic tension weakens the rock for frictional shear on horizontal planes. It should suppress *S* waves [*Tobita et al*., 2010]. That is, weakened *S* waves are expected to arrive during the tensile cycle of strong *P* waves.

With regard to data, station IWTH25 was nearly directly above the hypocenter of the 2008 Iwate-Miyagi earthquake. The body waves were essentially vertical and no apparent surface waves were recorded. *Yamada et al*. [2009], *Tobita et al*. [2010], and *Kinoshita* [2011] studied the asymmetry of *P* wave accelerations. As expected, upward accelerations are stronger than downward ones (Figure 10). *Tobita et al*. [2010] numerically modeled the suppression of *S* waves by *P* waves. There is a tendency of strong *S* waves to not arrive during strong tensional *P* waves (Figure 10).

5.2. Numerical Model

We present an idealized numerical model to illustrate the expected effects of *P* waves suppressing *S* waves in a half-space where shallow reverberations do not occur. The details are in Appendix B.

The parameters of our wave trains are arbitrary, but planned to illustrate key features of *S* wave suppression by *P* waves. We sent a pulse of seven *S* wave cycles from the bottom of our numerical domain to represent a long wave train with a period of 0.8 s. We let a continuous train of *P* waves with a period be 0.64 s impinge on the surface with an amplitude of 0.7 g. The *P* waves and *S* waves thus came in and out of phase. For simplicity, the *P* waves behaved linearly.

The (natural standard) top boundary condition was no tractions at the free surface, which reflects waves. Displacements were imposed at the bottom boundary to start the *S* waves. The bottom displacement was thereafter set to zero. The calculation was stopped before any reflected *S* waves reached bottom so this artificial boundary condition did not affect our numerical results.

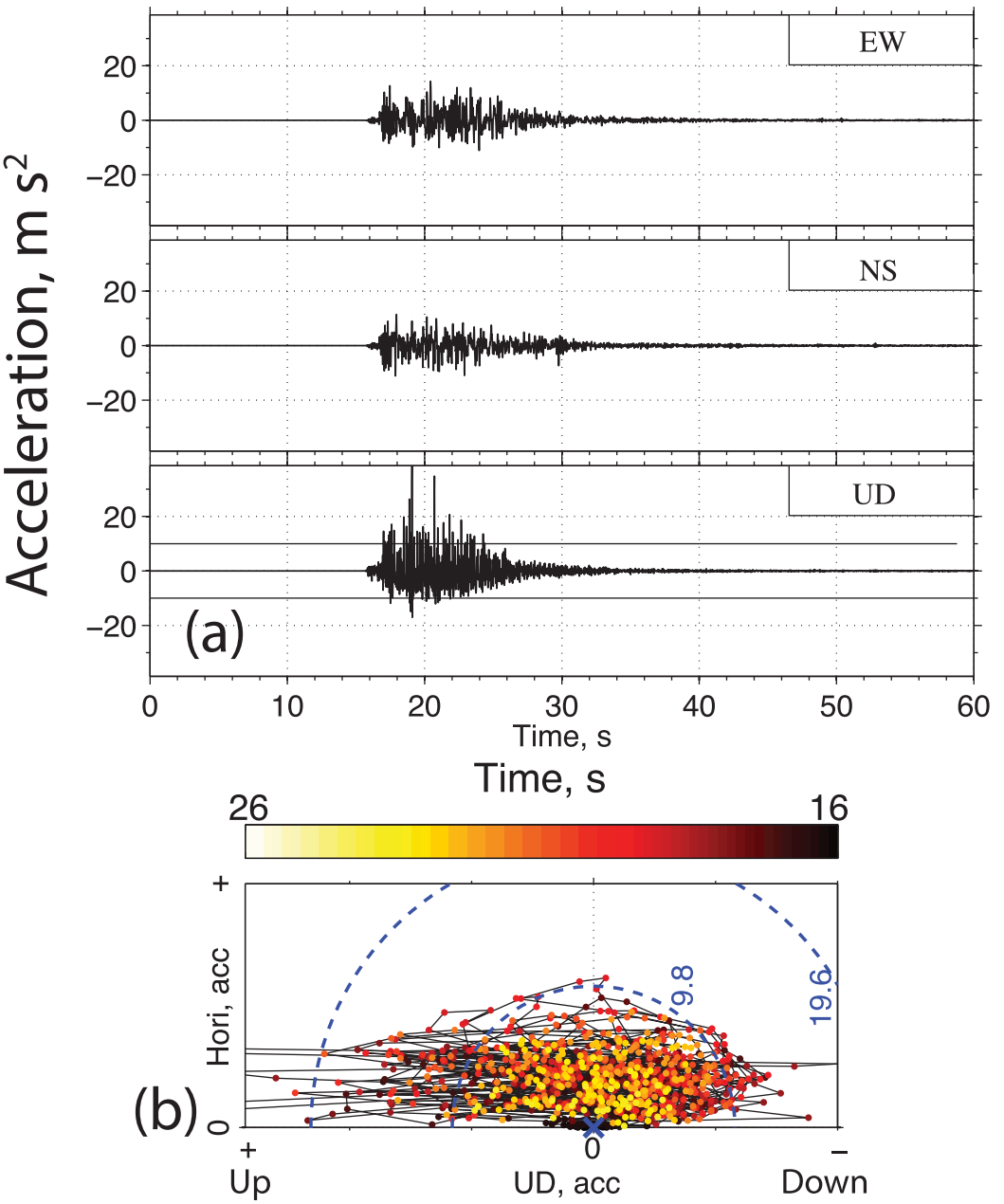

Figure 10. (a) The record at the surface station IWTH25 of the 2008 Iwate-Miyagi earthquake. Strong accelerations occur on the compressional phase of the vertical record. (b) Polar plot of the resolved horizontal acceleration with respect to the vertical acceleration. Circles of total acceleration of 1 and 2 g are shown for reference. The highest horizontal accelerations occur with weak vertical accelerations.

For simplicity, we select attenuation parameters suitable for dry exhumed sedimentary rock (see Appendix B). Our anelastic strain commences at a Coulomb ratio 0.3 and becomes faster with increasing Coulomb ratio.

We compare the waveform of linear waves with the numerically modeled waveform of nonlinearly attenuated waves. Our impinging *S* waves would produce accelerations of 0.8 g at the free surface if linear behavior occurred (Figure 11a). As expected from (16), nonlinear attenuation approximately clips *S* waves in the absence of *P* waves (Figure 11a). The peak value ~0.6 g defines an effective coefficient of friction for our model parameters.

As expected, strong tensile *P* wave amplitudes suppress *S* wave amplitudes as expected (Figure 11b). A subtle effect is the compressive cycles of *P* waves strengthen the subsurface for frictional sliding. Strong *S* waves do propagate the surface. Note that the acceleration must integrate to zero as the velocity eventually returns to zero.

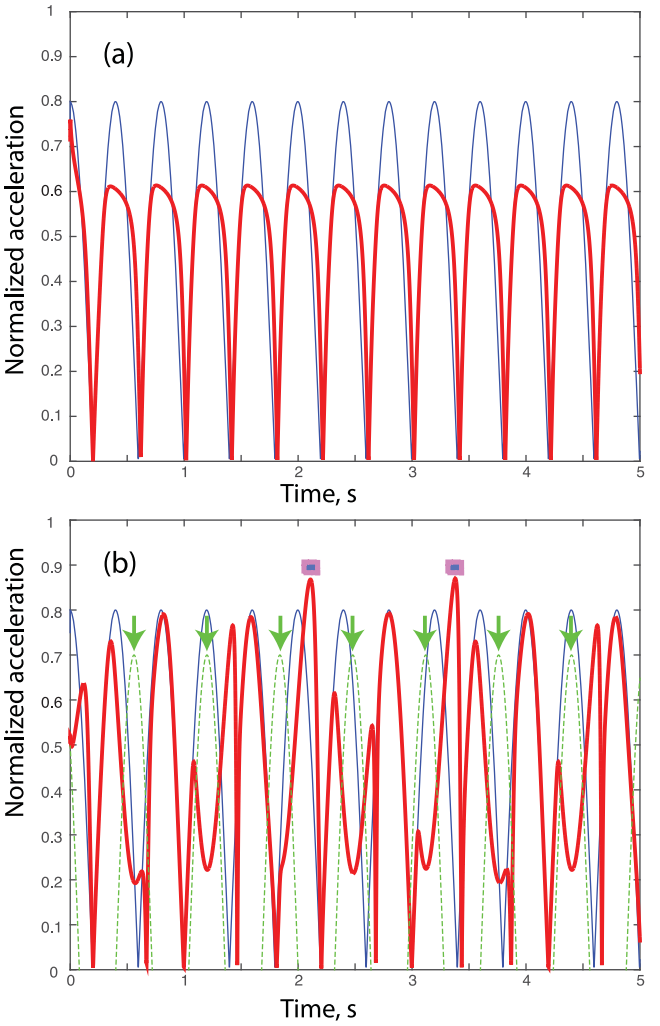

Figure 11. The computed absolute value of horizontal acceleration normalized to the acceleration of gravity from *S* waves (thick red line). The signal that would be produced in a linear material is shown for reference (thin blue line). (a) No *P* waves are present. The *S* waves clip at 0.6 g. (b) *P* waves with a peak acceleration of 0.7 g (dashed green line) arrive with the *S* waves. The *S* wave acceleration is suppressed at the times of peak downward acceleration (arrows). The *S* wave amplitude during the compressional phase of the *P* wave is sometimes slightly higher than that of the impinging signal (filled rectangles).

6. Interaction of High-Frequency *S* Waves With the Near-Field Velocity Pulse

We discussed in section 3.4 the modest effect of static coseismic stress changes at our Tohoku stations. We examine data from the 28 June 1992 Landers Mw 7.3 earthquake (Figure 12) where dynamic strain from the near-field velocity pulse likely caused high dynamic stresses within the stiff granite beneath a seismic station. In this case, nonlinear behavior likely occurred down to a few hundred meters depth.

We note that the strong near-field velocity pulse for the 2010 magnitude 8.8 Maule Chile earthquake coarrived with high-frequency *S* waves at Constitución [*Ruiz et al.*, 2012]. However, we do not know of any information on the subsurface velocity structure that would allow one to estimate dynamic stresses from the velocity pulse.

6.1. Observed Shaking at Lucerne

An analog station at Lucerne (LUC, located at 34.568°N, 116.612°W) recorded strong motions 1.25 km southwest of the nearest fault rupture of earthquake. *Iwan and Chen* [1995] and *Chen* [1995] obtained digital broadband records from the raw data. We use their digital horizontal records (Figure 12). *Sleep* [2012] recovered the digital vertical record from a plot file of their data that is not easily available from archives in numerical form. We retain the timing from these recovered records, but mildly adjust the absolute amplitude of the vertical acceleration.

The Lucerne seismograph was located on weathered granite above intact granite. We retain the physical properties from the seismic records and from unpublished data (R. Nigbor, personal communication, 2011) in the work of *Sleep* [2012]. The weathered layer is 13.5 m thick with *S* wave velocity of 400 m s^{-1} and *P* wave velocity of 693 m s^{-1} (*S* wave velocity times $\sqrt{3}$ keeping insignificant digits). The underlying granite has *S* wave velocity of 3000 m s^{-1} and P velocity $\sqrt{3}$ times this. We use the generic density of 2500 kg m^{-3} for both layers in example calculations.

The 1992 Landers event ruptured on a complicated series of faults in eastern California [e.g., *Wald and Heaton*, 1994; *Bouchon et al.*, 1998]. These works did not consider the Lucerne data, so we continue with the basic aspects of near-field pulses discussed by *Bouchon et al.* [1998].

The static displacement at Lucerne lasted from 6 to 20 s on the time scale in Figure 12 with most of the displacement between 8 and 18 s [*Iwan and Chen*, 1995; *Chen*, 1995]. The qualitative sequence of stress changes

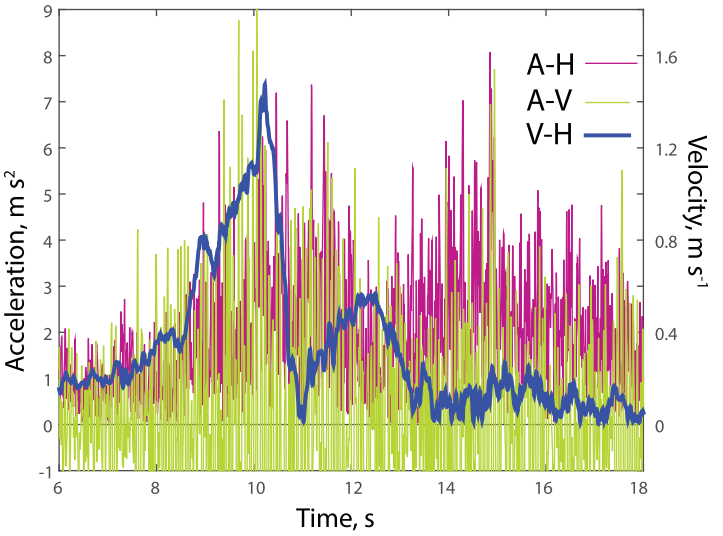

Figure 12. Resolved horizontal acceleration (thin green curves), resolved horizontal velocity (thick blue curves), and upward acceleration (thick red curves) at Lucerne. The velocity record from 6 to 18 s shows the near-field velocity pulse. The fault-parallel shear stress increased early on. The stress from the velocity may have been strongly antithetic to fault motion around 12.5 s; the amplitude of *S* waves was lower at that time.

is evident. The initial dynamic velocity augmented the ambient strike-slip tectonic stress ahead of the rupture tip approaching Lucerne. As a reality check, the combination of these stresses was large enough to produce off-fault failure elsewhere, where the rupture jumped between nearby faults [e.g., *Wald and Heaton*, 1994; *Bouchon et al.*, 1998]. Slip eventually occurred on the fault plane adjacent to Lucerne and decreased the fault-parallel shear traction. The static displacement at Lucerne ceased once fault slip moved farther away.

6.2. Dynamic Stresses Beneath Lucerne

We obtain scaling estimates of the static stress change in the underlying granite at Lucerne, from geodetic data. *Massonnet et al.* [1993] obtained surface displacements from InSAR data. The near-fault displacement varies by ~2 m over 5 km, giving a strain of $\sim 0.4 \times 10^{-3}$. The shear modulus of the underlying granite is 22.5 GPa, giving a stress change of 9 MPa.

With regard to dynamic stress, the velocity pulse likely propagated crudely at the *S* wave velocity of ~4000 m s^{-1} of deep intact granite. The scale strain V/β is 0.375×10^{-3}, giving a dynamic stress of 9 MPa using the maximum particle velocity V of ~1.5 m s^{-1}. For reference, treating the velocity pulse as an *S* wave in the 3000 m s^{-1} granite yields a scale stress $\rho V \beta$ of 11.25 MPa. As expected in the near field, the dynamic stress changes were comparable to the static ones.

We provide example calculation with realistic parameters for the Coulomb stress ratio. We assume the water table was deep at Landers and use the effective stress $\rho g z$ to estimate frictional properties for comparison with the dynamic stress estimates. The starting coefficient of friction in granite is not known. It could be from ~1 in locally mildly cracked domains to ~2 where intact [*Lockner*, 1995]. In these cases, frictional failure commences above a depth of 360 and 180 m, respectively, for 9 MPa of shear traction from the static strain. For reference, the typical wavelength of ~7 Hz *S* waves in Figure 12 is ~400 m. So at least a quarter-wavelength of seismic ray passed through granite that was likely nonlinear in friction.

In more detail, the granite responded to the tensor sum of the dynamic stress and the ambient strike-slip stress before event. We have no direct constraints on the ambient stress so we use a simple model of the earthquake cycle including frictional strength of shallow intact granite. Interseismic deep (partly elastic) deformation imposes displacements and strains on the shallow granite. The static strain in the earthquake reversed these strains and relaxed the shear traction on the fault. That is, interseismic strain has the sense to increase ambient tectonic stresses at shallow depths. The strain was large enough to bring shallow intact granite with a coefficient of friction of 2 into frictional failure. Overall, interseismic anelastic strain likely occurred with the upper few hundred meters of the granite. The rock was likely near frictional failure with strike-slip sense when the Landers event started.

6.3. Nonlinear Attenuation of High-Frequency *S* Waves

We make the inference from (10) that high-frequency *S* waves should nonlinearly attenuate when the granite was undergoing frictional failure because individual small slipping fractures did not distinguish among stresses from high-frequency *S* waves, stresses from the velocity pulse, and preexisting tectonic stresses.

We do not know much about the impinging *S* wave raypaths. The *S* wave velocity of the intact granite is fast, so the raypaths were not refracted into the vertical. Rays likely arrived in various directions from the fault plane. We proceed with a qualitative model.

The velocity record in Figure 12 is compatible the expected sequence of events at a near-field site [e.g., *Wald and Heaton*, 1994; *Bouchon et al*., 1998]. The observed amplitude of high-frequency *S* waves qualitatively correlates with our predictions. Dynamic frictional failure in the granite occurred ahead of the rupture tip during the initial part of the velocity pulse increased the shear stress from ~7 to ~9 s. The *S* waves attenuated nonlinearly and arrived with weak amplitudes. By ~9 s, the velocity pulse had reduced the tectonic shear stress so frictional failure in the granite beneath Lucerne had ceased. The *S* waves behaved more linearly and arrived at higher amplitudes at the surface. The dynamic shear stress likely brought the shallow subsurface into antithetic failure around ~12.5 s, again suppressing *S* waves. Strong *S* waves passed through low-stress granite from ~13 to ~17 s. Thereafter, fault rupture was too far away to produce strong accelerations.

Further quantification is difficult, as we do not have much information on the generation of high-frequency body waves and hence of the amplitude of waves arriving at a few hundred meters depth. Still, the sustained (low-frequency) acceleration of the near-field velocity pulse is a measure of moment generation, slip, and perhaps high-frequency wave production on the nearby fault. There is no obvious reason why early slip should have generated weak body waves and later slip generated strong body waves.

Milliner et al. [2015] studied along-strike near-fault static displacements the Landers faults. They inferred shallow anelastic strains accommodated ~46% of the macroscopic slip over a cross-strike width of ~154 m. Furthermore, direction detection of shallow anelastic behavior may be feasible with modern instruments. For example, strong shaking likely caused very shallow small earthquakes as at Parkfield [*Fischer et al*., 2008a, 2008b; *Fischer and Sammis*, 2009]. The Lucerne records are not optimal for searching for high-frequency pulses from such events. The seismograph was insensitive to signal above ~25 Hz [*Iwan and Chen*, 1995; *Chen*, 1995]. We do not have a viable recognition method for such energy bursts within the broadband frequency range of the main shock.

6.4. Caveats on Shallow Reverberations

As noted in section 6.1, a shallow (~13.5 deep) layer of low-velocity weathered granite exists beneath Lucerne. High-frequency body waves reverberated with near vertical paths within this layer. We discuss complications related to the reverberations with regard to analyzing *S* wave amplitudes.

First, *S* wave energy remained within the layer for ~0.5 s and *P* wave energy for ~0.3 s. These reverberations dominate acceleration records (Figure 12). The observed accelerations depend on the flux of energy from below averaged over these times [*Sleep*, 2012]. This effect is not a major issue for comparison of *S* wave amplitude with the slowly changing near-field velocity pulse.

A second effect arises because the signal is broadband and unpredictable [*Moustafa and Takewaki*, 2009; *Moustafa*, 2010]. *S* waves may come into phase at the surface and cause high accelerations but be out of phase at depth and not cause high stresses and nonlinear attenuation, or vice versa. With regard to wave types, the base of the weathered granite is irregular so there is some conversion of energy between *P* waves and *S* waves [*Sleep*, 2012]. The horizontal and vertical components do not fully separate the wave types.

Finally, there may be some tendency of strong high-frequency *P* waves to suppress *S* waves as discussed in section 5 (Figure 12). Weak *S* waves do occur as expected where *P* waves are strong near 9.5 s.

However, the existence of reverberations complicates straightforward interpretation. *S* wave energy loiters within the layer for a fraction of a second. Thus, the effect of suppression of *S* wave energy by a tensional *P* wave half-cycle will persist in the layer when the *P* wave becomes compressive. The usual issue with broadband signal arises: the deep stresses that cause nonlinear behavior are not fully in phase with the surface acceleration.

The overall amplitudes of *P* waves and *S* waves over a fraction of a second may be better measures of acceleration for considering nonlinear attenuation than the instantaneous peak amplitudes. Then there are far fewer independent samples for statistical analysis than when each peak amplitude behaves independently, as in the numerical model (Figure 11). We do not attempt to quantitatively model *S* wave with *P* wave interaction with the Lucerne data.

7. Discussion

We obtained analytical treatments for the nonlinear attenuation of strong seismic waves within rock from ~10 to a few hundred meters depth. This situation differs from the traditional engineering applications for shallow nonlinearity with ductile soil. Intuitively, rock should fail in friction. The form of the failure criterion, however, is not evident, especially when the normal traction on fractures and the mean stress change.

Frictional theories based on optimally oriented fractures (Figure 1) in (15) and those based on invariants of the stress tensor in a rock mass [*Drucker and Prager*, 1952] in (4) and (10) have been in wide use. For example, numerical models by *Roten et al.* [2014] employed *Drucker and Prager* [1952] plasticity. One of our objectives was to find field cases where analytical theory provided predictions that would allow one to sort out the appropriate frictional formalism. Our working testable assumption is that rocks masses do not distinguish among dynamic stresses from different classes of seismic waves and ambient tectonic stresses. We reiterate our field examples.

Rayleigh waves produce horizontal dynamic tension and compression at shallow depths. In the absence of tectonic stress, frictional failure occurs at a smaller dynamic stress change for tension than for compression (Figure 1). Attenuation from this failure would suppress the tensional half-cycle of Rayleigh waves. We did not observe this effect on records of Great Tohoku earthquake. Most likely the wave amplitudes were too feeble to bring the uppermost few hundred meters of the subsurface into frictional failure.

Rayleigh waves are also expected to interact with shallow ambient tectonic stresses. Failure would occur on the compressional half-cycle if the tectonic stress was so large that the rock was already near failure. We did not observe this effect on seismograms from Great Tohoku earthquake. It is conceivable that frictional failure during previous strong events had already relaxed the tectonic stress.

The strong 3–4 s Rayleigh waves might be expected to suppress high-frequency *S* waves. Here the predictions of theory based on horizontally oriented failure fractures differ from that of theory based on stress invariants. With regard to oriented fractures, shear waves cause horizontal shear traction on horizontal fractures. Rayleigh waves do not change the mean shear traction or the mean normal traction, on such shallow fractures. So no interaction is expected. However, both Rayleigh waves and *S* waves contribute to the shear invariant $|\tau|$ in (12). High-frequency *S* waves thus are expected to be suppressed at times of high Rayleigh wave particle velocity.

We noted in (19) and (20) that Rayleigh waves do not change the mean normal traction on shallow horizontal surfaces. The predicted failure envelope is thus an ellipse in high-frequency *S* wave acceleration, Rayleigh wave particle velocity space. Data from Japanese station MYGH05 were bounded by such an ellipse (Figure 9). The nonlinear behavior occurred at ~10 m depth.

The tensile cycle on strong *P* waves reduces the normal traction on horizontal planes. The frictional strength of these planes from the horizontal shear traction from strong *S* waves should be decreased. That is, strong *P* waves should suppress *S* waves as in Figure 10 for the 2008 Iwate-Miyagi earthquake.

The near-field velocity pulse ahead of the rupture tip in the 1992 Landers earthquake augmented ambient tectonic stress in the upper few under Lucerne. The increased stress brought the rock mass into friction failure. This interaction suppressed high-frequency *S* waves in Figure 12.

8. Conclusions

Sufficiently strong seismic waves should bring rock within the uppermost ten to few hundred meters into frictional failure. We have made the reasonable potentially testable hypothesis that fracture surfaces within rock do not distinguish between remote sources of traction. The combined effects of various classes of seismic waves and of ambient tectonic stresses bring fractures into failure. The predicted net effects of numerous fractures on the scale of the rock mass are anelastic strain and nonlinear attenuation.

Strong seismic waves of one class thus may suppress waves of another class. We presented mildly positive examples. Strong 3 s Rayleigh waves appear to have suppressed high-frequency *S* waves during the 2010 Great Tohoku earthquake. Strong high-frequency *P* waves suppressed high-frequency *S* waves during the

Iwate-Miyagi earthquake. The near-field velocity pulse suppressed high-frequency *S* waves during the 1992 Landers earthquake. These examples serve to illustrate the expected effects as an aid to appraising more examples. They are compatible with the occurrence of nonlinear effects, but are too poorly resolved to make detailed inferences about rock mechanical properties.

Appendix A: Dynamic Strain and Stress From Rayleigh Wave

We obtain the relationship between particle velocity and shallow dynamic stress for a Rayleigh wave from well-known wave equations. Our monochromic Rayleigh wave propagates in the *x* direction. The horizontal displacement at the surface is,

$$U_x = U_0 \exp\left[i(\omega t - kx)\right], \tag{A1}$$

where U_0 is the maximum horizontal displacement. This displacement varies slowly with depths $z \ll 1/k$. We use it to represent wave properties in the shallow subsurface. The shallow particle velocity is then

$$V_x = i\omega U_0 \exp\left[i(\omega t - kx)\right]. \tag{A2}$$

The longitudinal strain in the *x* direction is

$$\varepsilon_{xx} = \frac{\partial U_x}{\partial x} = -ikU_0 \exp\left[i(\omega t - kx)\right]. \tag{A3}$$

From (A2) and (A3), the maximum strain in the *x* direction is

$$\varepsilon_{\max} = \frac{V_{max}}{c_{\mathrm{Ray}}}, \tag{A4}$$

where $c_{\mathrm{Ray}} \equiv \omega/k$ is the phase velocity of the Rayleigh wave and $V_{max} \equiv |U_0\omega|$ is PGV. A particle velocity in the direction of wave propagation produces horizontal compression.

We obtain expressions for ambient static stress and dynamic stress from Rayleigh waves for application to frictional failure. The dynamic stresses τ_{xz} and τ_{zz} are zero at the free surface. The dynamic strain ε_{yy} perpendicular to the *xz* plane of particle motion is zero. The maximum horizontal dynamic stress from peak strain $\varepsilon_{\max}$ from ε_{xx} is then,

$$\Delta\sigma_{\max} = \varepsilon_{\max}\left[\frac{E}{(1-\nu^2)}\right] \approx \frac{8}{3}\varepsilon_{\max} G, \tag{A5}$$

where $E = 2(1+\nu)G$ is Young's modulus, $\nu = \lambda/2(\lambda+G)$ is Poisson's ratio, λ is the second Lamé constant, and the approximate equality assumes $\lambda = G$ [e.g., *Turcotte and Schubert*, 2002, p. 114]. For reference, the multiplicative constant is 4 in the limit of Poisson ratio of $^1/_2$.

We obtain the particle velocity at failure V_{fail} for optimally oriented fractures from (A5). The stress change for failure $\Delta\sigma_{\mathrm{fail}}$ in (1) equals the bracket in (1) times the effective vertical normal traction P_{eff},

$$\frac{8\rho\beta^2 V_{\mathrm{fail}}}{3c_{\mathrm{Ray}}} = \left[\frac{2\mu}{(1+\mu^2)^{1/2} \mp \mu}\right]\left[(\rho - \rho_w)gz\right], \tag{A6}$$

where the plus sign represents dynamic horizontal tension. Solving for the societal relevant quantity PGV at rock failure yields

$$V_{\mathrm{fail}} = \frac{3gBz(\rho - \rho_w)c_{\mathrm{Ray}}}{8\rho\beta^2}, \tag{A7}$$

where *B* is the term in the bracket in (A6). For comparison, the failure velocity of Love waves is

$$V_{\mathrm{Love}} = \frac{gz\mu(\rho - \rho_w)c_{\mathrm{Love}}}{\rho\beta^2}, \tag{A8}$$

where c_{Love} is the phase velocity of Love waves [*Sleep and Erickson*, 2014]. The ratio of these velocities is

$$\frac{V_{\text{fail}}}{V_{\text{Love}}} = \frac{3Bc_{\text{Ray}}}{8\mu c_{\text{Love}}}. \tag{A9}$$

Appendix B: Stresses and Nonlinearity of Body Waves Near the Free Surface

We obtain the relationship between dynamic acceleration and Coulomb stress ratios in the shallow subsurface. For simplicity, we first present the results for *S* waves. Particle motion is only in the *x* horizontal direction. With the long duration of *S* wave shaking in Figures 4 and 5 in mind, we represent a wave train of long duration as sinusoidal oscillation with a single frequency within a half-space. We present formulas for stress from shallow *S* waves for application to frictional failure. Reflection of an upgoing wave from the free surface produces a downgoing wave so that the shear traction τ is zero at the free surface. The displacement *U* in the *x*-direction is

$$U = U_0[\cos(\omega t + kz) + \cos(\omega t - kz)], \tag{B1}$$

and the shear traction on horizontal planes is

$$\tau = G\frac{\partial U}{\partial z} = -GkU_0[sin(\omega t + kz) - sin(\omega t - kz)] = -2U_0 Gkcos(\omega t)sin(kz), \tag{B2}$$

where $2U_0$ is the peak scalar displacement at the free surface $z=0$, z is depth, k is wave number, ω is angular frequency, and G is the shear modulus. The *S* wave velocity $\beta = \omega/k = \sqrt{G/\rho}$ where ρ is density. The final equality gives the expression for a standing wave that shows that shallow stress is in phase with surface displacement and surface acceleration.

The quarter-wavelength depth and the scale depth $1/k$ provide convenient length scales for frictional failure. Stress reaches its overall maximum of $2\tau_0 \equiv 2GkU_0 = 2\rho V_0\beta$ at the quarter wavelength depth $\pi/(2k)$, where V_0 is the maximum particle velocity. For an isolated propagating wave $U = U_0\cos(\omega t \pm kx)$, the maximum scalar stress is $\rho V_0\beta$ and the maximum dynamic strain is V_0/β. At shallow depths where $kz < 1$, the first term of the Taylor series expansion of (B2) yields the well-known result that the peak shear stress is

$$|\tau| = 2U_0k^2Gz = 2\rho V_0\beta kz = 2\rho A_0 z, \tag{B3}$$

where A_0 is the maximum acceleration.

To the first order, vertically propagating *S* waves cause frictional failure on horizontal planes. The effective stress is $(\rho - \rho_w)gz$. The frictional failure criterion then implies that the dynamic stress will be bounded by $|\tau| \le (\rho - \rho_w)\mu gz$, where μ is the coefficient of friction. In the region near the free surface where (B3) applies, the maximum peak ground acceleration (PGA) is predicted to be bounded by the frictional failure criterion,

$$\frac{2A_0}{g} \le \left(\frac{(\rho - \rho_w)}{\rho}\right)\mu \equiv \mu_{\text{eff}}. \tag{B4}$$

At failure, the peak normalized ground acceleration in is $2A_0/g$ [e.g., *Hartzell et al.*, 2004, p. 1614]. The second equality defines the effective coefficient of friction μ_{eff}. Nonlinear attenuation would tend to clip on normalized acceleration at this level if the rock failed in friction.

The *S* waves in our data are broadband (Figure 8). We discuss application of (B4) to such data. We represent the displacement, as upgoing and downgoing kinematic waves $U_x = U_0[H(\beta t + z) + H(\beta t - z)]$, where H is an arbitrary well-behaved function. The velocity at $z=0$ is the time derivative $2\beta U_0 H'(\beta t)$. The acceleration is $A = 2\beta^2 U_0 H''(\beta t)$, which is twice the acceleration that the upgoing wave would produce alone. The stress at the very shallow depth δz depends on the spatial derivative $\tau = U_0 G[H'(\beta t + \delta z) - H'(\beta t - \delta z)]$, which goes to zero at the free surface. In the limit of $\delta z \to 0$, the shear traction is $2U_0 G\delta z H''(\beta t)$. Noting that $G = \rho\beta^2$ recovers (B4).

That is, the stress ratio on the right-hand side of (B4) applies at the free surface where normal traction and shear traction approach 0. However, the frictional limit on acceleration in (B4) is unlikely to apply at extremely shallow depths. Real rocks are likely to have some cohesive strength at zero normal traction and

real seismographs are moored to the ground with finite strength. Thus nonlinear attenuation occurs at a finite depth with the highest stresses being around the quarter wavelength depth. The stress τ at depth is statistically but not simply to the surface acceleration. We use the envelope function in (17) to obtain a stable prediction of shallow stress from measured surface acceleration.

The derivation of dynamic stresses for vertical *P* waves is analogous to that for vertical *S* waves in (B4). The dynamic vertical pressure change from a monochromic *P* wave reflecting from a free surface is in analogy with (B2),

$$-P_{zz}=(\lambda+2G)\frac{\partial U_P}{\partial z}=-(\lambda+2G)k_P U_P[sin(\omega t+k_P z)-sin(\omega t-k_P z)]$$
$$=-2(\lambda+2G)k_P U_P cos(\omega t)sin(k_P z), \tag{B5}$$

where the *P* wave velocity is $\alpha=\sqrt{(\lambda+2G)/\rho}$ and the subscript *P* indicates properties of the *P* wave. The relationships between dynamic pressure and acceleration for *S* waves in (B3) and (B4) carry through. The ratio of dynamic pressure change to lithostatic pressure is proportional to the normalized surface acceleration with downward acceleration producing dynamic tension. Downward acceleration weakens horizontal planes in friction while downward acceleration strengthens them.

The interaction of vertical *S* waves with *P* waves is simple enough to model with code modified from that of *Sleep and Erickson* [2014]. This code applies to a homogeneous half-space. We retain their physical parameters appropriate to shallow Los Angeles Basin sediments: The *S* wave velocity is 500 m s^{-1} and the *P* wave velocity $\sqrt{3}$ times this. Density is 2250 kg m^{-3}. We let the anelastic strain per time step (Δt=0.002 s over 1 m grid) function be

$$\Delta\varepsilon=\varepsilon'\Delta t=\zeta\left[\frac{\tau_M}{G}\right]\left[\frac{|\tau\{t_0\}|-\tau_B}{\tau_M}\right]^M, \tag{B6}$$

where anelastic strain has the sign to relieve stress, ζ=1 is a dimensionless constant, $\tau_M=\rho g\mu_M z$ is a stress where frictional creep becomes fast at the Coulomb stress ratio μ_M=0.8; $\tau_B=\rho g\mu_B z$ implies that no anelastic strain occurs below a Bingham coefficient of friction of μ_B=0.3 ($\varepsilon'=0; |\tau| \le \tau_B$), and *M*=5 is an exponent that represents modestly rapid transition between slow and fast deformation as dynamic stress increases. There is no frictional creep below a Coulomb stress ratio of 0.3. The intent is to represent the net behavior of a rock mass with numerous fractures with different frictional strengths and different prestresses. The transition from elasticity to plasticity is gradual as in (10) and (11). We replaced in the code *g* with $g+a_P$, where a_P is the imposed local *P* wave acceleration.

Acknowledgments
Marine Denolle, Greg Beroza, and Eric Dunham promptly answered questions. Two anonymous reviewers and the Associate Editor provided helpful comments. This research was supported by the Southern California Earthquake Center. SCEC is funded by NSF Cooperative Agreement EAR-0106924 and USGS Cooperative Agreement 02HQAG0008. The SCEC contribution for this paper is SCEC Publications Database. The KiK-net data are publically available from National Research Institute for Earth Science and Disaster Prevention (NIED). The horizontal components of the Lucerne data are available from Cosmos. The vertical Lucerne data are not currently easily obtainable in digital form from archives, but are available in analog form from cited references.

References

Aoi, S., T. Kunugi, and H. Fujiwara (2008), Trampoline effect in extreme ground motions, *Science*, *322*, 727–730.
Assimaki, D., W. Li, and A. Kalos (2011), A wavelet-based seismogram inversion algorithm for the in situ characterization of nonlinear soil behavior, *Pure Appl. Geophys.*, *168*, 1669–1691, doi:10.1007/s00024-010-0198-6.
Bouchon, M., M. Campillo, and F. Cotton (1998), Stress field associated with the rupture of the 1992 Landers, California, earthquake and its implications concerning the fault strength at the onset of the earthquake, *J. Geophys. Res.*, *103*(B9), 21,091–21,097.
Bradley, B. A., and M. Cubrinovski (2011), Near-source ground motions observed in the 22 February 2011 Christchurch earthquake, *Seismol. Res. Lett.*, *82*(6), 853–865.
Bullen, K. E., and B. A. Bolt (1985), *An Introduction to the Theory of Seismology*, 4th ed., 499 pp., Cambridge Univ. Press, Cambridge, U. K.
Chen, X. (1995), Near-field ground motion from the Landers Earthquake, PhD thesis, 147 pp., Calif. Inst. of Technol., Pasadena.
Dieterich, J. H. (1979), Modeling of rock friction: 1. Experimental results and constitutive equations, *J. Geophys. Res.*, *84*(B5), 2161–2168.
Drucker, D. C., and W. Prager (1952), Soil mechanics and plastic analysis or limit design, *Q. Appl. Math.*, *10*, 157–165.
Fischer, A. D., and C. G. Sammis (2009), Dynamic driving of small shallow events during strong motion, *Bull. Seismol. Soc. Am.*, *99*, 1720–1729.
Fischer, A. D., C. G. Sammis, Y. L. Chen, and T.-L. Teng (2008a), Dynamic triggering by strong motion P- and S-waves: Evidence from 1999 Chi-Chi, Taiwan Earthquake, *Bull. Seismol. Soc. Am.*, *98*, 580–592.
Fischer, A. D., Z. G. Peng, and C. G. Sammis (2008b), Dynamic triggering of high-frequency bursts by strong motions during the 2004 Parkfield earthquake sequence, *Geophys. Res. Lett.*, *35*, L12305, doi:10.1029/2008GL033905.
Frankel, A. (2013), Rupture History of the 2011 M 9 Tohoku Japan Earthquake determined from strong-motion and high-rate GPS recordings: Subevents radiating energy in different frequency bands, *Bull. Seismol. Soc. Am.*, *103*, 1290–1306.
Hartzell, S., L. F. Bonilla, and R. A. Williams (2004), Prediction of nonlinear soil effects, *Bull. Seismol. Soc. Am.*, *96*, 1609–1629.
Hasegawa, A., K. Yoshida, Y. Asano, T. Okada, T. Iinuma, and Y. Ito (2012), Change in stress field after the 2011 great Tohoku-Oki earthquake, *Earth Planet. Sci. Lett.*, *355–356*, 231–243.
Headquarters for Earthquake Research Promotion (2011), Long-term evaluation of active faults, Ministry of Education, Culture, Sports, Science and Technology, Tokyo, Japan. [Available at http://www.jishin.go.jp/main/p_hyoka02_danso.htm.]

Iwan, W. D., and X. Chen (1995), Important near-field ground motion data from the Landers earthquake, in *10th European Conference on Earthquake Engineering*, edited by G. Duma, pp. 229–234, A. A. Balkema, Rotterdam, Netherlands.
Jaeger, J. C., N. G. W. Cook, and R. W. Zimmerman (2007), *Fundamentals of Rock Mechanics*, 475 pp., Blackwell, Malden, Mass.
Jana, P., and A. Chatterjee (2013), Modal damping in vibrating objects via dissipation from dispersed frictional microcracks, *Proc. R. Soc. A*, *469*, doi:10.1098/rspa.2012.0685.
Kinoshita, S. (2011), A stochastic approach for evaluating the nonlinear dynamics of vertical motion recorded at the IWTH25 site for the 2008M_w 6.9 Iwate–Miyagi Inland Earthquake, *Bull. Seismol. Soc. Am.*, *101*, 2955–2966.
Kjartansson, E. (1979), Constant Q-wave propagation and attenuation, *J. Geophys. Res.*, *84*(B9), 4737–4748, doi:10.1029/JB084iB09p04737.
Kohli, A. H., and M. D. Zoback (2013), Frictional properties of shale reservoir rocks, *J. Geophys. Res. Solid Earth*, *118*, 5109–5125, doi:10.1002/jgrb.50346.
Linker, M. F., and J. H. Dieterich (1992), Effects of variable normal stress on rock friction: Observations and constitutive equations, *J. Geophys. Res.*, *97*(B4), 4923–4940.
Lockner, D. A. (1995), Rock failure, in *Rock Physics and Phase Relations: A Handbook of Physical Constants, AGU Ref. Shelf Ser.*, vol. 3, edited by T. J. Ahrens, pp. 127–147, AGU, Washington, D. C., doi:10.1029/RF003p0127.
Lubliner, J. (1990), *Plasticity Theory*, 495 pp., Macmillan, N. Y.
Massonnet, D., M. Rossi, C. Carmona, F. Adragna, G. Peltzer, K. Feigl, and T. Rabaute (1993), The displacement field of the Landers earthquake mapped by radar interferometry, *Nature*, *364*, 138–142.
Milliner, C. W. D., J. F. Dolan, J. Hollingsworth, S. Leprince, F. Ayoub, and C. G. Sammis (2015), Quantifying near-field and off-fault deformation patterns of the 1992 M_w 7.3 Landers earthquake, *Geochem. Geophys. Geosyst.*, *16*, 1577–1598, doi:10.1002/2014GC005693.
Minato, S., T. Tsuji, S. Ohmi, and T. Matsuoka (2012), Monitoring seismic velocity change caused by the 2011 Tohoku-oki earthquake using ambient noise records, *Geophys. Res. Lett.*, *39*, L09309, doi:10.1029/2012GL051405.
Moustafa, A. (2010), Identification of resonant earthquake ground motion, *Sādhanā*, *35*(3), 355–371.
Moustafa, A., and I. Takewaki (2009), Use of probabilistic and deterministic measures to identify unfavorable earthquake records, *J. Zhejiang Univ. Sci. A*, *10*(5), 619–634.
Nakata, N., and R. Snieder (2011), Near-surface weakening in Japan after the 2011 Tohoku-Oki earthquake, *Geophys. Res. Lett.*, *38*, L17302, doi:10.1029/2011GL048800.
Nakata, N., and R. Snieder (2012a), Estimating near-surface shear wave velocities in Japan by applying seismic interferometry to KiK-net data, *J. Geophys. Res.*, *117*, B01308, doi:10.1029/2011JB008595.
Nakata, N., and R. Snieder (2012b), Time-lapse change in anisotropy in Japan's near surface after the 2011 Tohoku-Oki earthquake, *Geophys. Res. Lett.*, *39*, L11313, doi:10.1029/2012GL051979.
Nishida, K., H. Kawakatsu, and K. Obara (2008), Three-dimensional crustal S wave velocity structure in Japan using microseismic data recorded by Hi-net tiltmeters, *J. Geophys. Res.*, *113*, B10302, doi:10.1029/2007JB005395.
Perfettini, H., J. Schmittbuhl, J. R. Rice, and M. Cocco (2001), Frictional response induced by time-dependent fluctuations of the normal load, *J. Geophys. Res.*, *106*(B7), 13,455–13,472.
Roten, D., K. B. Olsen, S. Day, Y. Cui, and D. Fäh (2014), Expected seismic shaking in Los Angeles reduced by San Andreas Fault zone plasticity, *Geophys. Res. Lett.*, *41*, 2769–2777, doi:10.1002/2014GL059411.
Ruina, A. (1983), Slip instability and state variable laws, *J. Geophys. Res.*, *88*(B12), 10,359–10,370.
Ruiz, S., R. Madariaga, M. Astroza, G. R. Saragoni, M. Lancieri, C. Vigny, and J. Compos (2012), Short-Period Rupture Process of the 2010 M_w 8.8 Maule Earthquake in Chile, *Earthquake Spectra*, *28*(S1), S1–S18.
Sawazaki, K., and R. Snieder (2013), Time-lapse changes of *P*- and *S*-wave velocities and shear wave splitting in the first year after the 2011 Tohoku earthquake, Japan: Shallow subsurface, *Geophys. J. Int.*, *193*, 238–251.
Simons, M., et al. (2011), The 2011 magnitude 9.0 Tohoku-oki earthquake: Mosaicking the megathrust from seconds to centuries, *Science*, *332*, 1421–1425, doi:10.1126/science.
Sleep, N. H. (2011), Seismically damaged regolith as self-organized fragile geological feature, *Geochem. Geophys. Geosyst.*, *12*, Q12013, doi:10.1029/2011GC003837.
Sleep, N. H. (2012), Site resonance from strong ground motions at Lucerne, California, during the 1992 Landers mainshock, *Bull. Seismol. Soc. Am.*, *102*, 1505–1513.
Sleep, N. H. (2014), Ambient tectonic stress as fragile geological feature, *Geochem. Geophys. Geosyst.*, *15*, 3628–3644, doi:10.1002/2014GC005426.
Sleep, N. H., and B. A. Erickson (2014), Nonlinear attenuation of S-waves and Love waves within ambient rock, *Geochem. Geophys. Geosyst.*, *15*, 1419–1440, doi:10.1002/2014GC005250.
Sleep, N. H., and P. Hagin (2008), Nonlinear attenuation and rock damage during strong seismic ground motions, *Geochem. Geophys. Geosyst.*, *9*, Q10015, doi:10.1029/2008GC002045.
Sleep, N. H., and S. Ma (2008), Production of brief extreme ground acceleration pulses by nonlinear mechanisms in the shallow subsurface, *Geochem. Geophys. Geosyst.*, *9*, Q03008, doi:10.1029/2007GC001863.
Tobita, T., S. Iai, and T. Iwata (2010), Numerical analysis of near-field asymmetric vertical motion, *Bull. Seismol. Soc. Am.*, *100*(4), 1456–1469.
Toda, S., J. Lin, and R. S. Stein (2011), Using the 2011 M_w 9.0 off the Pacific coast of Tohoku Earthquake to test the Coulomb stress triggering hypothesis and to calculate faults brought closer to failure, *Earth Planets Space*, *63*, 725–730.
Townend, J., and M. D. Zoback (2000), How faulting keeps the crust strong, *Geology*, *28*, 399–402.
Turcotte, D. L., and G. Schubert (2002), *Geodynamics*, 2nd ed., 456 pp., John Wiley, N. Y.
Wald, D. J., and T. H. Heaton (1994), Spatial and temporal distribution of slip for the 1992 Landers, California, earthquake, *Bull. Seismol. Soc. Am.*, *84*(3), 668–691.
Wang, J., C. Xu, J. T. Freymueller, Z. Li, and W. Shen (2014), Sensitivity of Coulomb stress change to the parameters of the Coulomb failure model: A case study using the 2008 M_w 7.9 Wenchuan earthquake, *J. Geophys. Res. Solid Earth*, *119*, 3371–3392, doi:10.1002/2012JB009860.
Wu, C., and Z. Peng (2011), Temporal changes of site response during the 2011 M_w 9.0 off the Pacific coast of Tohoku Earthquake, *Earth Planets Space*, *63*, 791–795.
Wu, C., and Z. Peng (2012), Long-term change of site response after the M_w 9.0 Tohoku earthquake in Japan, *Earth Planets Space*, *64*, 1259–1266.
Yamada, M., J. Mori, and T. Heaton (2009), The slapdown phase in high-acceleration records of large earthquakes, *Seismol. Res. Lett.*, *80*(4), 559–564.

Yang, Y.-R., K. M. Johnson, and R. Y. Chuang (2013), Inversion for absolute deviatoric crustal stress using focal mechanisms and coseismic stress changes: The 2011M9 Tohoku-oki, Japan, earthquake, *J. Geophys. Res. Solid Earth*, *118*, 5516–5529, doi:10.1002/jgrb.50389.

Yoshida, K., A. Hasegawa, T. Okada T. Iinuma, Y. Ito, and Y. Asano (2012), Stress before and after the 2011 great Tohoku-oki earthquake and induced earthquakes in inland areas of eastern Japan, *Geophys. Res. Lett.*, *39*, L03302, doi:10.1029/2011GL049729.

Zoback, M. D., and J. Townend (2001), Implications of hydrostatic pore pressures and high crustal strength for the deformation of intra-plate lithosphere, *Tectonophysics*, *336*, 19–30.

Zoback, M. D., J. Townend, and B. Grollimund (2002), Steady-state failure equilibrium and deformation of intraplate lithosphere, *Int. Geol. Rev.*, *44*, 383–401.